

4 Results

4.1 Tensile Data

Tensile tests were performed in an Instron tensile test machine in air at 316°C and a strain rate of $\approx 4 \times 10^{-4} \text{ s}^{-1}$ in accordance with ASTM Specifications E8 and E21. The cross-head movement and digitized load were recorded as a function of time. The strain was calculated based on the cross-head deflection.

4.1.1 Alloy 600 from CRDM Nozzle #3 and Alloy 182 from the Nozzle #11 J-Groove Weld

The engineering stress vs. strain curves for Alloy 600 from the Davis-Besse CRDM Nozzle #3 are shown in Fig. 34, and those for Alloy 182 from Nozzle #11 J-groove weld are shown in Fig. 35. The values of yield and ultimate stresses, elongation, and reduction in area are given in Table 8. The stress vs. strain curves for the three Alloy 600 specimens from the nozzle show excellent agreement (Fig. 34). The results for the Alloy 182 specimens from the J-groove weld show some differences, which are caused either by flaws in the material or the entire gauge length not consisting of the weld metal alone in the specimen.

Table 8. Tensile test results at 316°C for Alloys 600 and 182 removed from the Davis-Besse CRDM nozzle and J-groove weld.

Specimen ID (Alloy Type)	0.2% Yield Stress (MPa)	Ultimate Stress (MPa)	Elongation (%)	Reduction in Area (%)
N3TL-1 (A 600)	290	549	62.3	51.8
N3TL-2 (A 600)	250	548	67.9	54.1
N3TL-3 (A 600)	283	549	63.8	54.0
J11TC-1 (A 182)	390	580	24.6	38.4
J11TC-2 (A 182)	420	587	24.6	58.2
J11TL-2 (A 182) sub-size	346	555	47.8	47.3
J11TL-3 (A 182) sub-size	356	532	36.6	38.0
J11TL-4 (A 182) sub-size	350	420	11.8	14.1

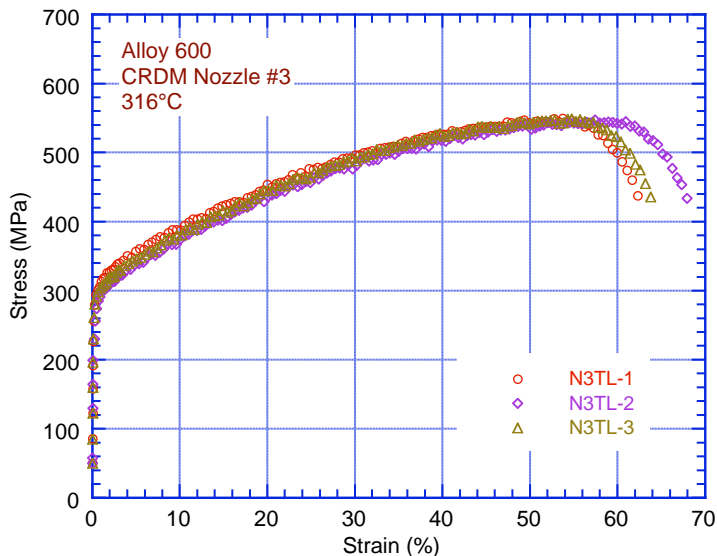


Figure 34. Engineering stress vs. strain curve at 316°C for Alloy 600 from Davis-Besse CRDM Nozzle #3 in the “L” orientation.

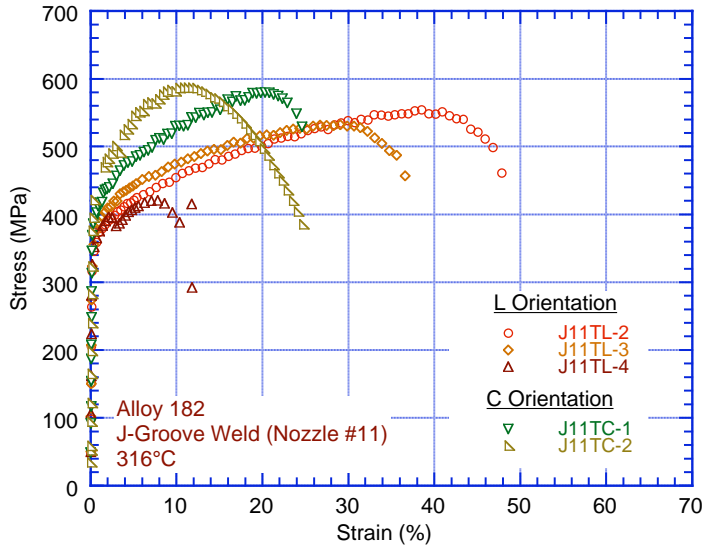


Figure 35. Engineering stress vs. strain curves at 316°C for Alloy 182 from the Davis-Besse CRDM Nozzle #11 J-groove weld in “L” and “C” orientations.

The stress vs. strain curves for two Alloy 182 specimens in the L orientation are comparable (J11TL-2 and -3), but the third specimen (J11TL-4) showed poor ductility because of a large flaw (Fig. 36 a). The stress vs. strain curves for Alloy 182 specimens in the C orientation are significantly different from those in the L orientation. The gauge section near the specimen shoulder of C-orientation specimens contained a small region of the reactor vessel head material. In both C-orientation specimens, fracture occurred in this region; e.g., half of the fracture surface is low-alloy steel in J11TC-1 (Fig. 36b) and all of the fracture surface in J11TC-2 (Fig. 36c). In Specimen J11TC-1, because the soft and hard regions appear to be parallel and approximately of similar areas on the cross section, its stress-vs.-strain curve should be representative of the tensile behavior of the J-groove Alloy 182 in the C orientation. The total elongation for Specimen J11TC-2 can probably not be considered representative.

The tensile strength of the Alloy 182 J-groove weld is higher and the ductility is lower than the corresponding properties for the Alloy 600 nozzle material. For the Alloy 182 weld, the strength is slightly higher and the ductility is lower in the C orientation than in the L orientation.

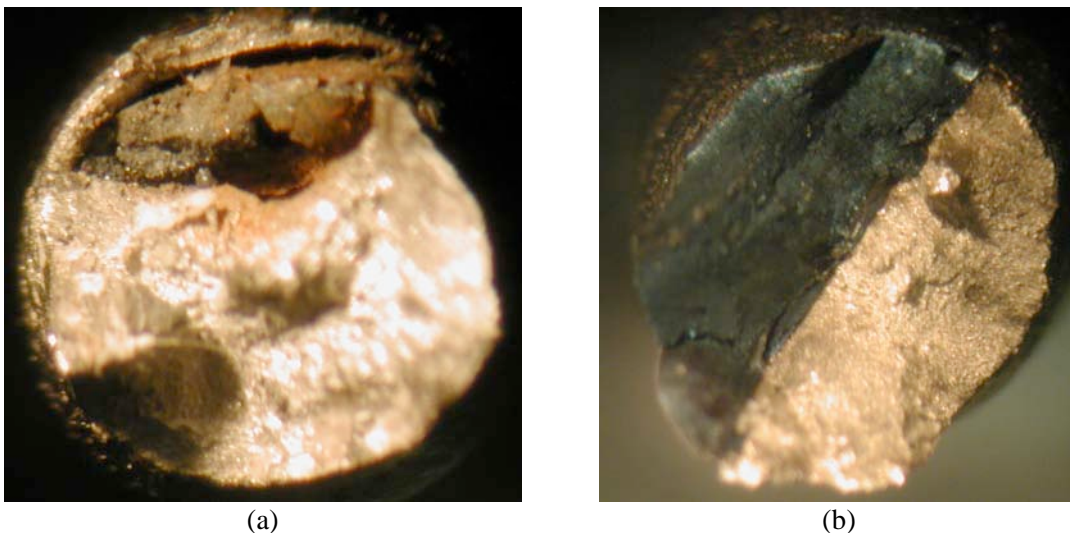


Figure 36. Fracture surfaces of Alloy 182 Specimens (a) J11TL-4, (b) J11TC-1, and (c) J11TC-2 from the Davis-Besse CRDM Nozzle #11 J-groove weld.



(c)

Figure 36. (Contd.)

4.1.2 Alloys 82 and 182 from the V.C. Summer Nozzle-to-Pipe Weld and Butter

The engineering stress vs. strain curves for Alloy 182 and 82 specimens from the butter and weld regions of the V.C. Summer nozzle-to-pipe dissimilar metal weld are shown in Fig. 37. The values of the yield and of the ultimate stresses and elongation are given in Table 9. The yield and ultimate strengths of Alloy 182 specimens from the butter region of the V.C. Summer weld are higher than those of Alloy 82 specimens from the weld region. This difference in tensile strength may be due to differences in the orientation of the dendritic structure and not to differences in alloy composition. The dendrites are parallel to the stress axis in the weld specimens and transverse to the stress axis for the butter specimens.

Table 9. Tensile test results at 316°C for Alloys 182 and 82 removed from the V.C. Summer nozzle-to-pipe dissimilar metal weld.

Specimen ID (Alloy Type)	0.2% Yield Stress (MPa)	Ultimate Stress (MPa)	Elongation (%)
WTC-1 (A 82) weld region	320	535	52.6
WTC-2 (A 82) weld region	392	547	42.1
BTC-1 (A 182) butter region	430	662	37.4
BTC-2 (A 182) butter region	424	629	32.9

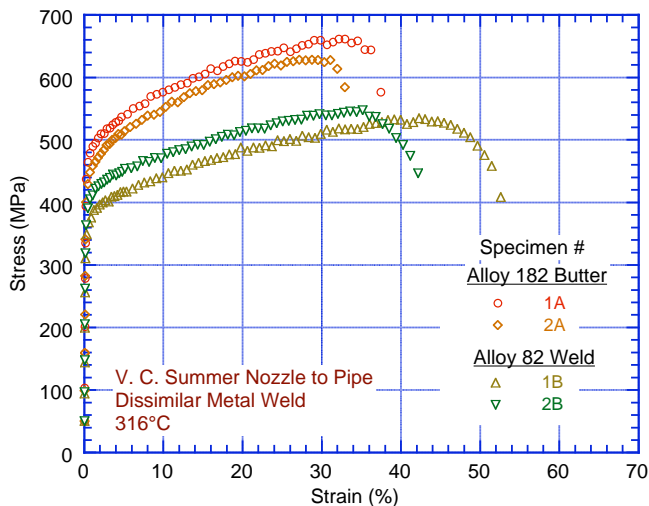


Figure 37. Engineering stress vs. strain curves at 316°C for Alloy 182 and 82 specimens from the butter and weld regions of the V.C. Summer nozzle-to-pipe dissimilar metal weld.

4.2 Crack Growth Data

4.2.1 Davis–Besse CRDM Nozzle Alloy 600

Crack growth tests have been conducted on 1/4–T CT specimens in L and C orientations (N3CL–1 and N3CC–2, respectively) and 1/2–T CT specimen (N3CC–3) in the C orientation.

4.2.1.1 Specimen N3CL-1

The test conditions, experimental CGRs, the allowed K_{max} from the K /size criterion, and the margin between the applied and allowed K_{max} are given in Table 10. The ECPs of a Pt electrode and a companion Alloy 600 electrode located downstream from the autoclave were -584 and -585 mV, respectively. Fatigue precracking was carried out at $R \approx 0.3$, $K_{max} \approx 20$ MPa·m^{1/2}, and triangular waveform with 2–10 Hz frequency. After precracking, R was increased incrementally to 0.5, and the loading waveform was changed to a slow/fast sawtooth with rise time of 30, 300, or 1000 s. The changes in crack length and K_{max} with time during various test periods are shown in Fig. 38. The allowable K_{max}

Table 10. CGR data for 1/4–T CT Specimen N3CL-1 of Alloy 600 in PWR water at 316°C.

Test Period	Test Time (h)	Conductivity (μS/cm) ^a	R Load Ratio	Rise Time (s)	Down Time (s)	Hold Time (s)	K _{max} (MPa·m ^{1/2})	ΔK (MPa·m ^{1/2})	Growth Rate (m/s)	Allowed K _{max} (MPa·m ^{1/2})	K _{app} – K _{max} (%)	Crack Length (mm)
Pre a	51	21.0	0.26	1	1	0	20.0	14.8	5.07E-09	20.3	-1	5.993
Pre b	71	–	0.28	5	5	0	19.4	14.0	3.09E-09	20.1	-3	6.117
1	115	–	0.53	30	4	0	21.2	9.9	4.30E-10	19.9	6	6.199
2	194	18.5	0.54	300	4	0	21.5	9.9	2.55E-10	19.9	8	6.240
3a	225	18.5	0.52	300	4	0	22.7	10.9	8.88E-11	19.8	15	6.269
3b	316	14.7	0.51	300	4	0	24.5	12.0	2.63E-10	19.7	25	6.353
4	436	12.8	0.71	300	4	0	25.3	7.3	1.10E-10	19.6	29	6.400
5	676	15.4	0.70	1000	12	0	24.5	7.3	negligible	19.6	25	6.398
6	722	15.4	0.51	300	4	0	25.1	12.3	4.42E-10	19.5	29	6.471
7a	818	13.0	0.50	1000	12	0	24.6	12.3	5.45E-11	19.4	27	6.493
7b	868	13.0	0.51	1000	12	0	25.6	12.5	3.73E-10	19.3	33	6.562

^aRepresents values in the effluent. Feedwater conductivity was about the same as in the effluent. Water flow rate was 50 cc/min.

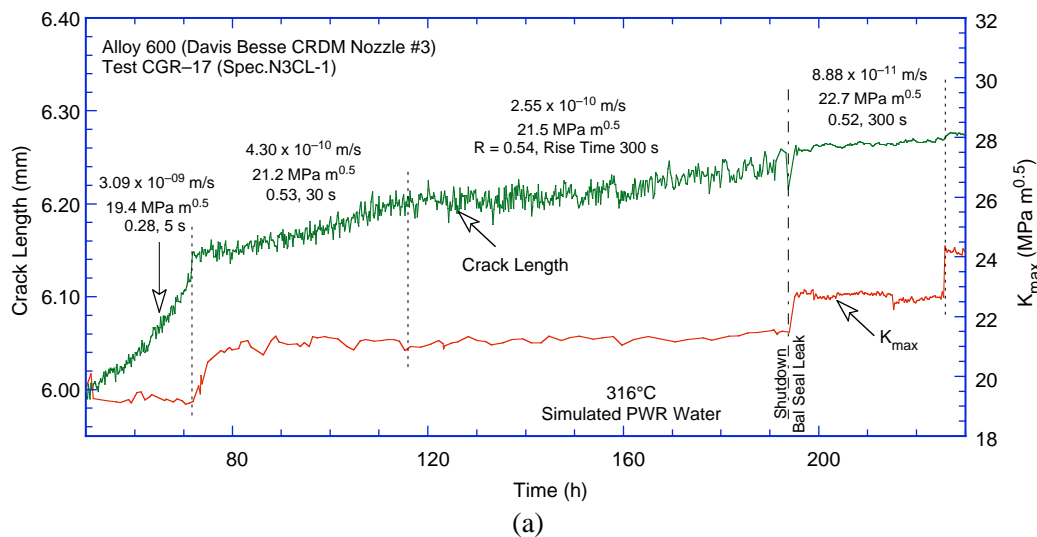
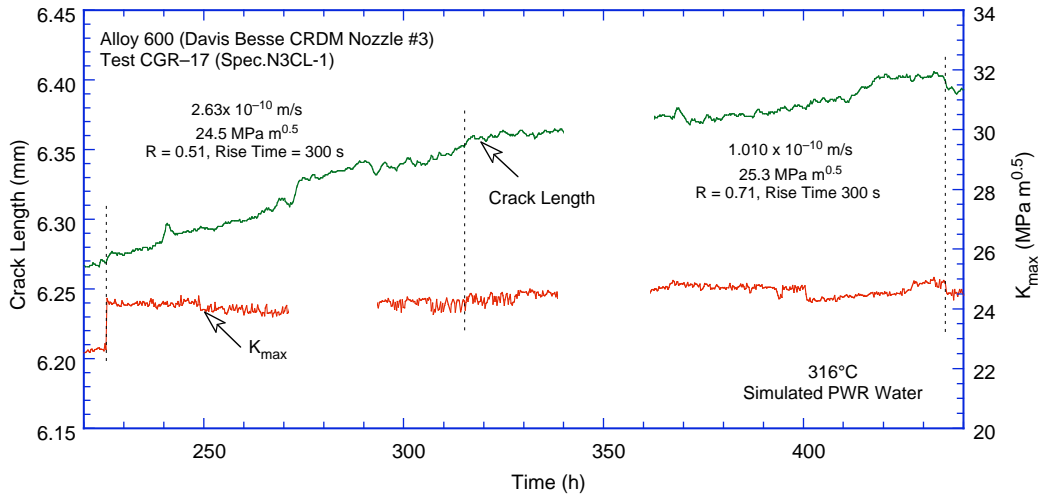
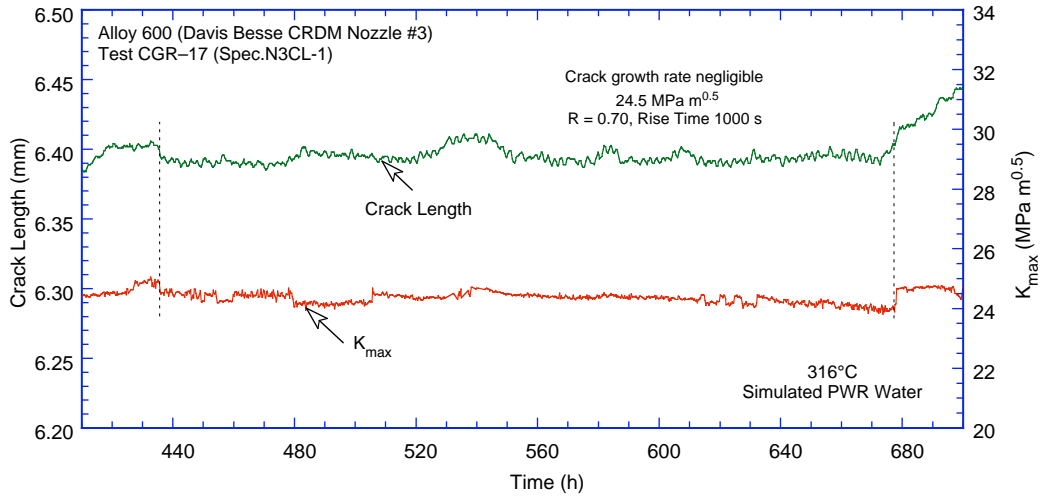


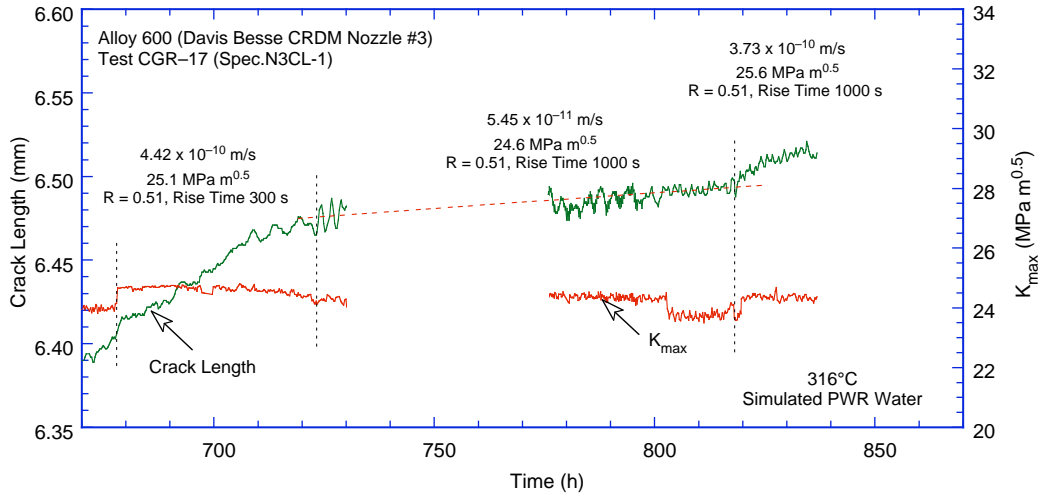
Figure 38. Crack length vs. time for Specimen N3CL-1 in simulated PWR environment at 320°C during test periods (a) precracking–2, (b) 3–4, (c) 5, and (d) 6–7.



(b)



(c)



(d)

Figure 38. (Contd.)

was calculated from Eq. 12 using flow stress rather than yield stress. For this specimen, the constant-load CGRs were not obtained because at 840 h the CGR increased abruptly by a factor of 5. It was assumed that the applied K_{\max} exceeded the value allowed by the K/size criterion, and the test was terminated.

A micrograph covering the entire fracture surface is shown in Fig. 39. The fracture mode was completely IG for all testing periods. The actual crack extension was 83% greater than the value determined from the DC potential drop measurements for this specimen. This difference most likely is due to the presence of secondary cracks and unbroken ligaments on the fracture surface. The crack extensions estimated from the DC potential method were scaled proportionately in both Table 10 and Fig. 38. While for the noncorrected values, the applied K_{\max} was within the limits set by the K/size criterion, and the correction resulted in applied K_{\max} factors $\approx 20\%$ larger than maximum allowed by the criterion for most of the test periods.

One unusual feature was the observation of IG fracture very early in the test, e.g., even during precracking (Fig. 39). The fracture mode during precracking at low load ratios and high frequency is generally transgranular (TG). The fracture morphology in the Davis–Besse CRDM nozzle alloy changed from TG to IG when the fatigue crack encountered the very first grain boundary (Figs. 40a and b). In some regions, IG fracture occurred right from the machine notch (Fig. 40a).

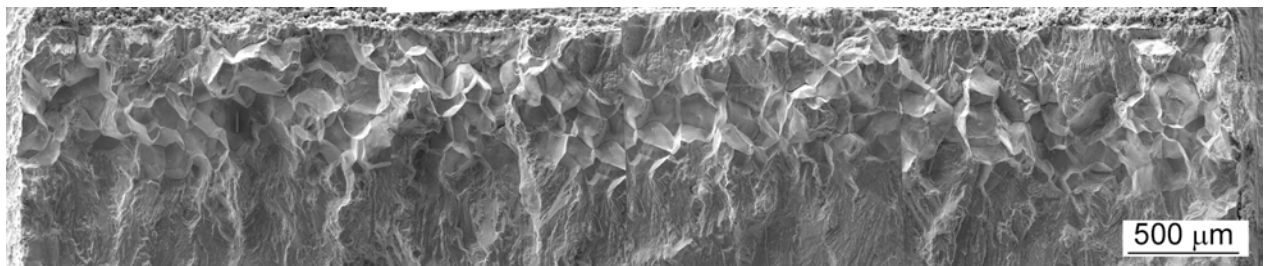


Figure 39. Micrograph of the fracture surface of Specimen N3CL-1. Crack advance is from top to bottom.

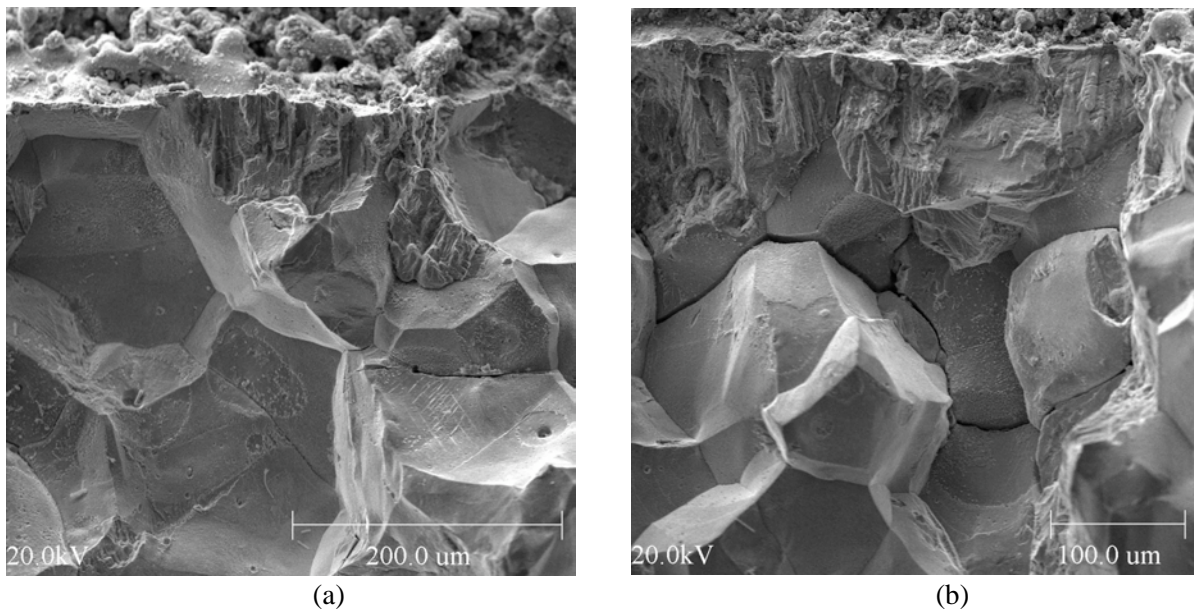


Figure 40. Examples of transition from a TG to an IG fracture mode in Specimen N3CL-1.

4.2.1.2 Specimen N3CC-2

Fatigue precracking was carried out at $R \approx 0.3$, $K_{\max} \approx 23 \text{ MPa}\cdot\text{m}^{1/2}$, and triangular waveform with 1–0.1 Hz frequency. After $\approx 0.16 \text{ mm}$ (6 mil) crack extension, R was increased incrementally to 0.5, and the loading waveform changed to a slow/fast sawtooth with a rise time of 30 or 300 s. The test conditions, experimental CGRs, the allowed K_{\max} from K/size criterion, and the margin between the applied and allowed K_{\max} are given in Table 11. The changes in crack length and K_{\max} with time during various test periods are shown in Fig. 41. For this test, the ECPs of the Pt electrode and the companion Alloy 600 electrode, located downstream from the autoclave, were -706 and -704 mV , respectively. The test was interrupted at $\approx 1220 \text{ h}$ because of a leak. The test was restarted at $R \approx 0.5$, $K_{\max} \approx 24.5 \text{ MPa}\cdot\text{m}^{1/2}$, and a slow/fast sawtooth waveform with a 300-s rise time.

Table 11. CGR data for 1/4-T CT Specimen N3CC-2 of Alloy 600 in PWR water at 316°C.

Test Period	Test Time (h)	Conductivity ^a ($\mu\text{S}/\text{cm}$)	R Load Ratio	Rise Time (s)	Down Time (s)	Hold Time (s)	K_{\max} ($\text{MPa}\cdot\text{m}^{1/2}$)	ΔK ($\text{MPa}\cdot\text{m}^{1/2}$)	Growth Rate (m/s)	Allowed K_{\max} ($\text{MPa}\cdot\text{m}^{1/2}$)	$K_{\text{app}} - K_{\max}$ (%)	Crack Length (mm)
Pre a	189	22	0.31	5	5	0	23.1	15.9	7.52E-10	19.9	16	6.243
1	383	20	0.51	300	4	0	22.3	10.9	2.13E-11	19.8	12	6.270
2	457	17	0.51	30	4	0	22.9	11.2	6.05E-11	19.7	16	6.335
3	550	16	0.51	300	4	0	22.8	11.2	9.46E-12	19.7	16	6.338
4	580	15	0.51	30	4	0	24.9	12.2	8.59E-10	19.6	27	6.415
5	765	15	0.50	300	12	0	24.8	12.4	8.87E-11	19.5	28	6.471
6	885	15	0.70	300	12	0	25.0	7.5	5.28E-11	19.4	29	6.492
7	912	16	0.51	300	12	0	25.1	12.3	1.01E-10	19.4	29	6.502
8	1197	20	0.52	300	12	3600	25.7	12.4	6.92E-11	19.3	33	6.541
9	1365	21	0.48	300	12	0	24.6	12.8	7.53E-11	19.2	28	6.617
10	1530	21	1.00	–	–	–	24.7	–	9.67E-11	19.1	29	6.658

^aRepresents values in the effluent. Feedwater conductivity was about the same as in the effluent. Water flow rate was 42 cc/min.

The fracture surface of Specimen N3CC–2 is shown in Fig. 42. As in the previous test, the fracture mode was completely IG for all test periods; the fracture started as TG but changed to IG almost at the first grain boundary encountered. A slice of the entire crack extension is shown in Fig. 43a, and typical fracture morphology at select locations on the surface is shown in Figs. 43b and c. The precrack area at location A shows TG fracture only up to the nearest grain boundary, and location B shows smooth IG

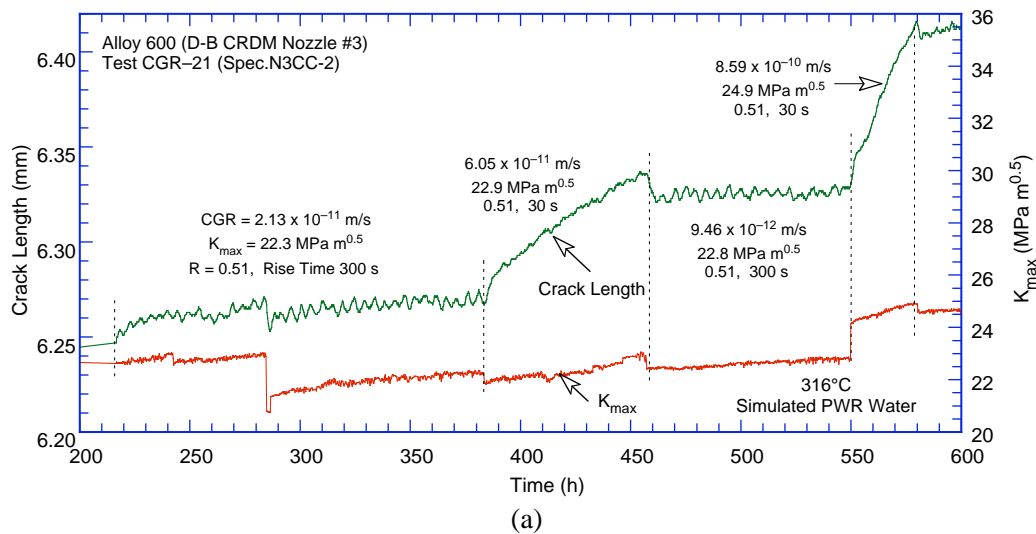


Figure 41. Crack length vs. time for Specimen N3CC-2 in a simulated PWR environment at 320°C during test periods (a) 1–4, (b) 5–8, and (c) 10–11.

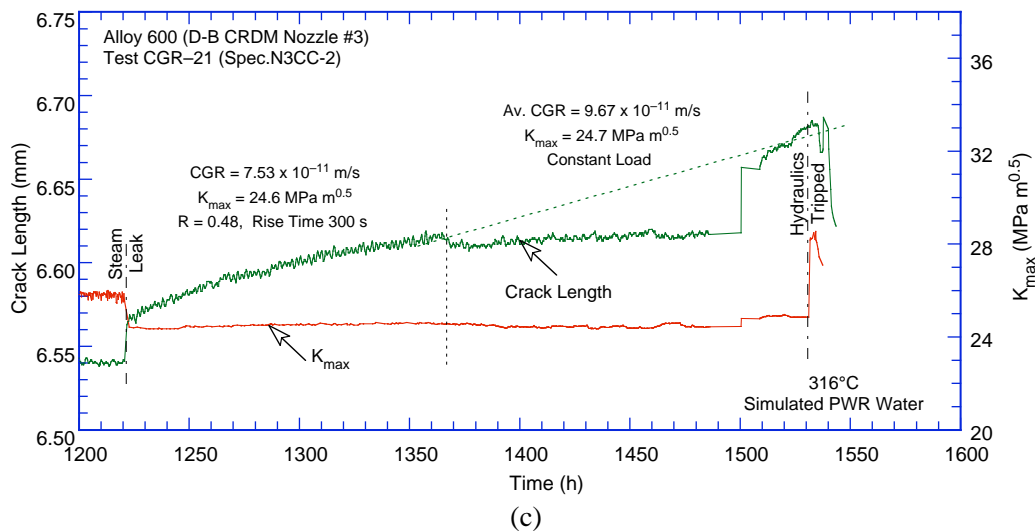
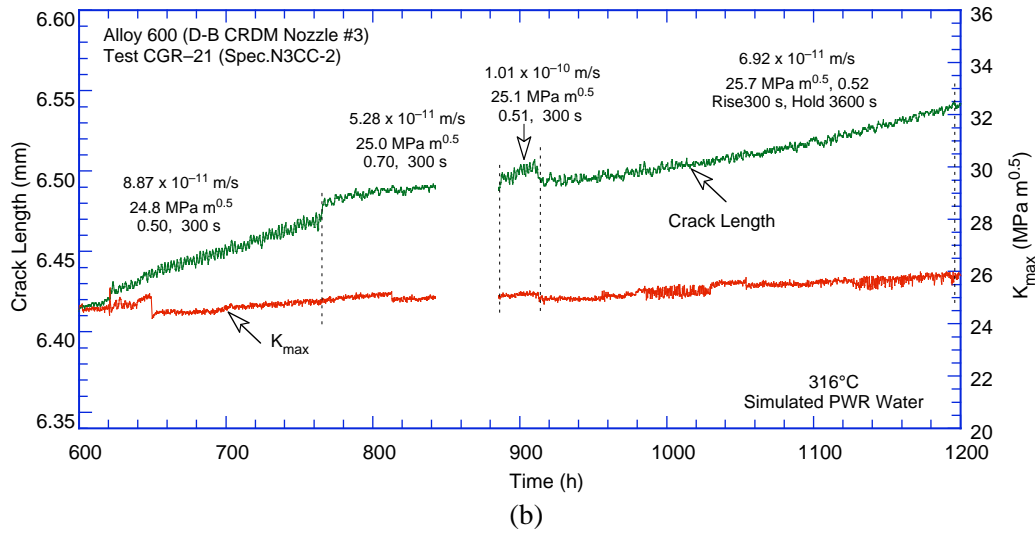


Figure 41. (Contd.)

fracture. The Ti-rich precipitates on the surface in Fig. 43c do not seem to affect the fracture mode. While the focus of this study was not on the effect of the Ti carbides on the SCC behavior of the alloy at hand, these particles can have a negative impact. As such, the precipitation of Ti carbides can reduce the concentration of free carbon retained in the matrix to a level at which it limits the precipitation of the desirable grain boundary chromium carbides. In addition, if Ti carbides precipitate at grain boundaries, they oxidize when exposed to the high-temperature water environment, possibly leading to grain boundary embrittlement.

The actual crack extension was 74% greater than the value determined from the DC potential drop method. Crack extensions estimated from the DC potential method were scaled proportionately; the corrected values of K_{max} and growth rate are given in Table 11. The results in Tables 10 and 11 indicate that for Specimens N3CL-1 and N3CC-2, the applied K_{max} for most of the test periods was $\approx 20\%$ higher than the value allowed by the K/size criterion.

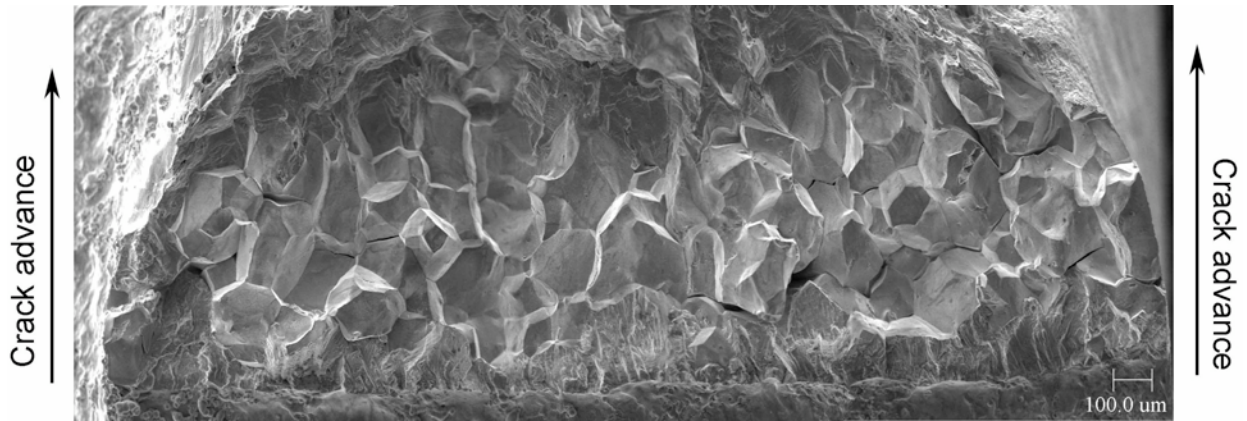


Figure 42. Micrograph of the fracture surface of Specimen N3CC-2. Crack advance is from bottom to top.

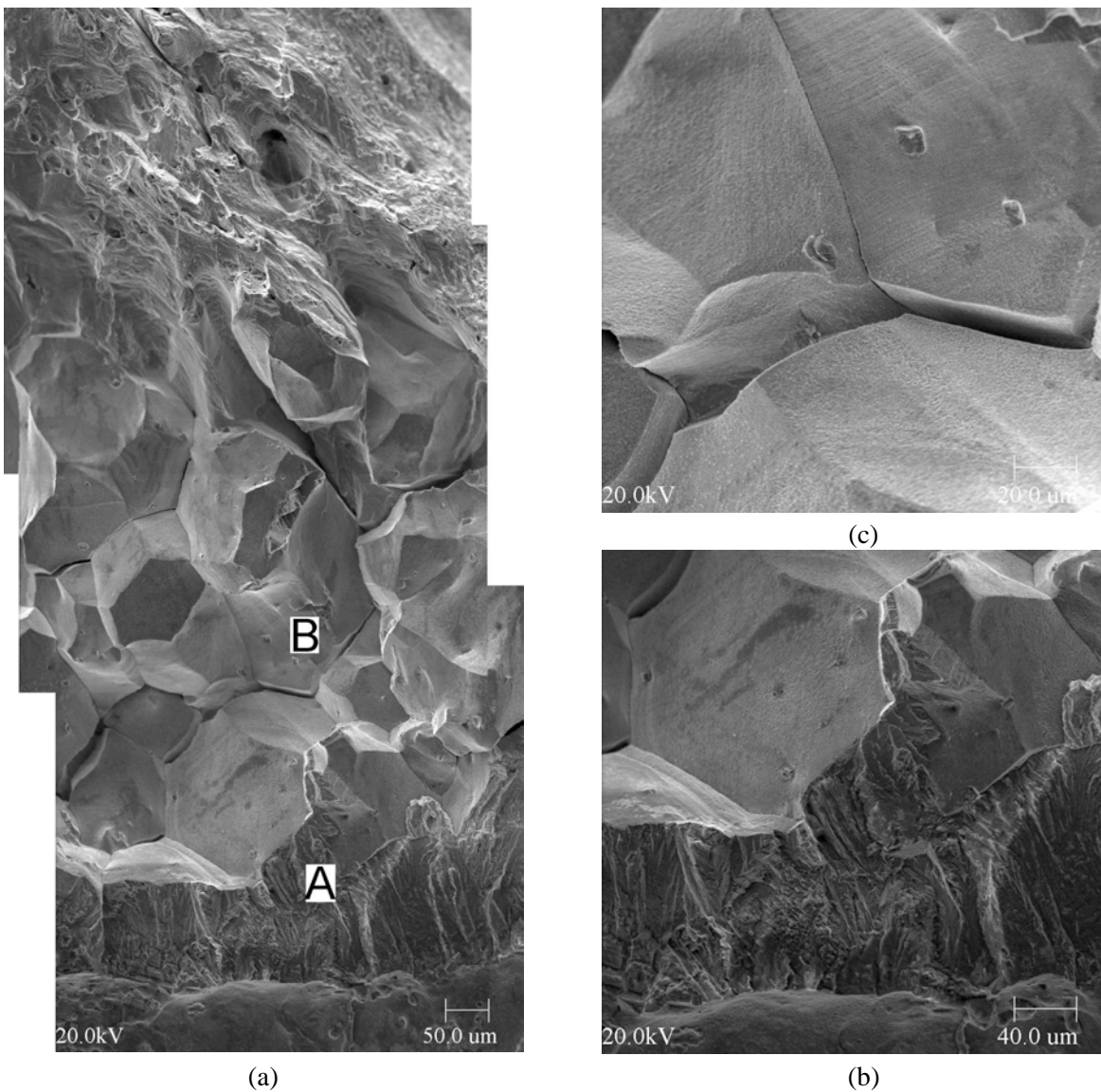


Figure 43. (a) Fracture surface of Specimen N3CC-2 and high-magnification micrographs at locations (b) A and (c) B.

4.2.1.3 Specimen N3CC-3

Testing for this specimen was carried out in a fashion similar to that of the previous two Alloy 600 specimens from Davis-Besse. However, unlike the previous two specimens, N3CC-3 was a 1/2-T CT specimen. Fatigue precracking was carried out at $R \approx 0.3$, $K_{\max} \approx 20 \text{ MPa}\cdot\text{m}^{1/2}$, triangular waveform, and frequency of 2 or 0.1 Hz. After an ≈ 0.3 – (12–mil) crack extension, R was increased incrementally to 0.5, and the loading waveform changed to a slow/fast sawtooth with rise time of 60 or 300 s. The test was interrupted at $\approx 530 \text{ h}$ when the strain limit tripped the test, causing the specimen to overstrain. The test was restarted under the loading conditions prior to the interruption. However, no crack growth was observed even after 120 h, and the test was terminated. The changes in crack length and K_{\max} with time are given in Table 12 and plotted in Fig. 44. The ECPs of the Pt electrode and the companion Alloy 600 electrode, located downstream from the autoclave, were -565 and -563 mV , respectively.

Table 12. CGR data for Specimen N3CC-3 in PWR water^a at 316°C.

Test Period	Test Time (h)	Conductivity ^b ($\mu\text{S}/\text{cm}$)	R Load Ratio	Rise Time (s)	Down Time (s)	Hold Time (s)	K_{\max} ($\text{MPa}\cdot\text{m}^{1/2}$)	ΔK ($\text{MPa}\cdot\text{m}^{1/2}$)	Growth Rate (m/s)	Allowed K_{\max} ($\text{MPa}\cdot\text{m}^{1/2}$)	$K_{\text{app}} - K_{\max}^c$ (%)	Crack Length (mm)
Pre a	50	20	0.36	0.25	0.25	0	20.8	13.3	1.35E-08	27.6	-25	12.777
Pre b	55	20	0.35	0.25	0.25	0	20.2	13.1	8.41E-09	27.5	-26	12.872
Pre c	72	19	0.33	5.0	5.0	0	19.9	13.3	2.03E-09	27.4	-27	12.943
Pre d	78	19	0.32	0.5	0.5	0	20.7	14.1	1.31E-08	27.2	-24	13.065
1	97	18	0.50	12	4	0	20.6	10.3	9.08E-10	27.1	-24	13.157
2	122	18	0.49	60	4	0	20.8	10.6	3.55E-10	27.1	-23	13.186
3	147	18	0.48	300	4	0	20.9	10.9	2.80E-10	27.1	-23	13.206
4	174	17	0.63	1,000	12	0	21.2	7.8	2.18E-10	27.0	-22	13.249
5a	230	16	1.00	-	-	-	20.5	0.00	7.85E-11	27.1	-24	13.218
5b	339	15	1.00	-	-	-	20.9	0.00	1.25E-10	26.9	-22	13.319
6a	386	14	1.00	-	-	-	26.4	0.00	2.28E-10	26.8	-2	13.404
6b	529	12	1.00	-	-	-	26.7	0.00	1.55E-10	26.7	0	13.510
7	648	12	1.00	-	-	-	31.9	0.00	negligible	26.5	20	13.637

^aSimulated PWR water with 2 ppm Li, 1000 ppm B, and ≈ 2 ppm dissolved hydrogen. Effluent DO was < 10 ppb.

^bRepresents values in the effluent.

^cBased on flow stress.

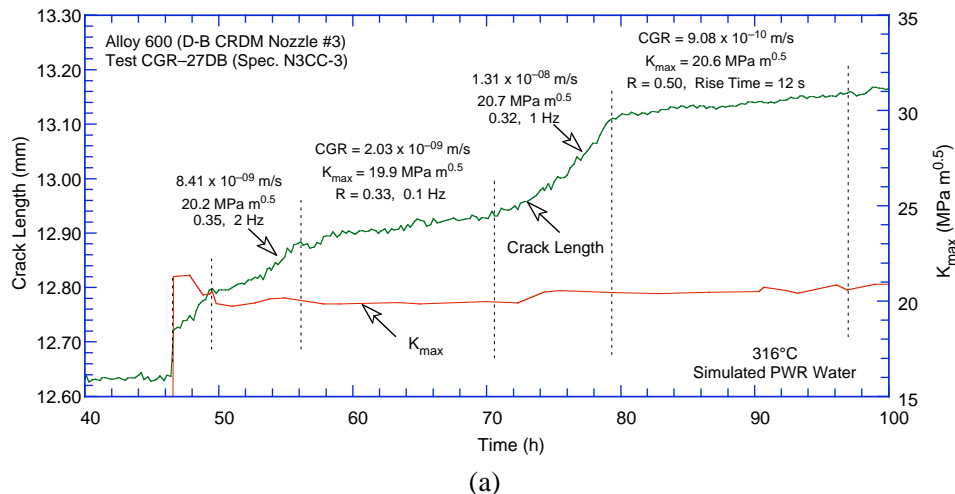


Figure 44. Crack length vs. time plots for Specimen N3CC-3 of Alloy 182 in PWR water at 316°C during test periods (a) precracking–1, (b) 2–5, and (c) 6–7.

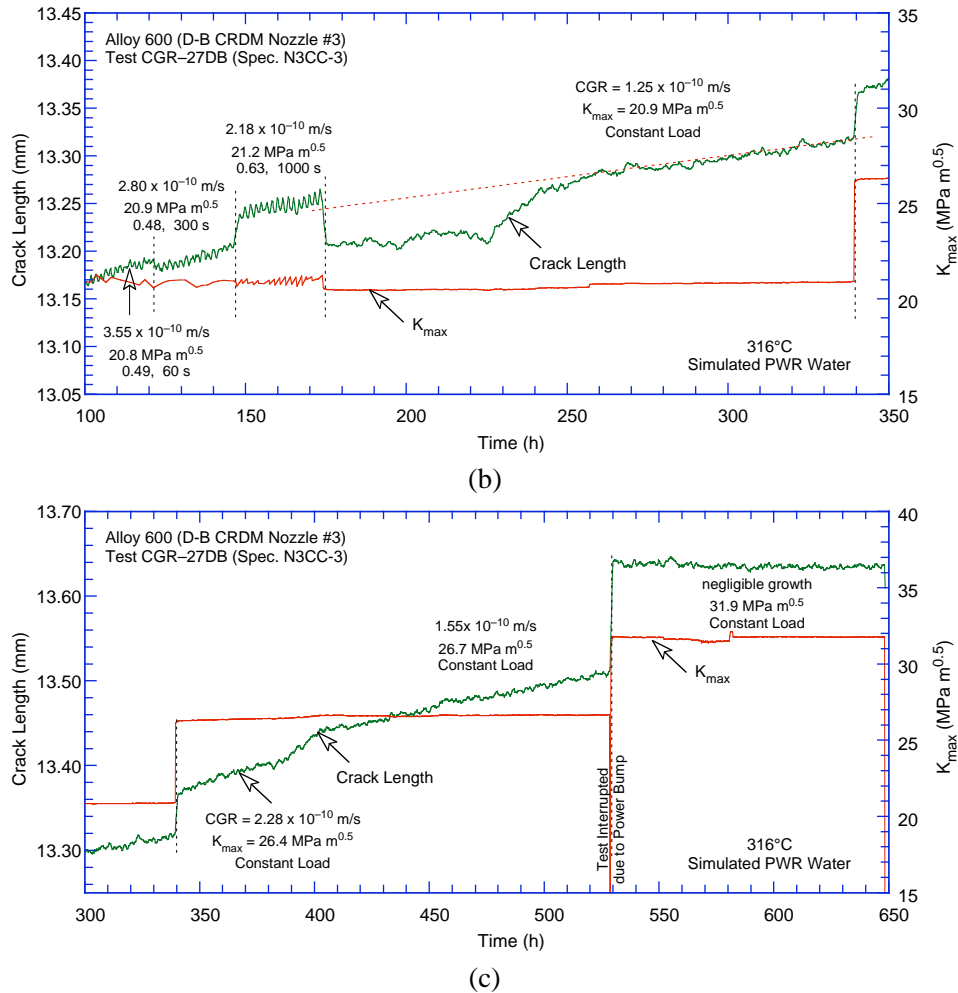


Figure 44. (Contd.)

After the test, the final crack size was marked by fatigue cycling in air at room temperature. The specimen was then fractured, and the fracture surface was examined in the SEM. Figure 45 shows the entire fracture surface. The beginning of the IG region is shown with green, and the end of the test is shown with red. Also shown, with yellow, are regions of smooth IG fracture in the initial TG region. The final crack advance was measured from the SEM micrograph in Fig. 45. The actual crack length was $\approx 57\%$ greater than the value determined from the DC potential measurements. The experimental crack extensions were scaled proportionately. The corrected test results, allowed K_{max} from K /size values, and the margins between the applied and allowed K_{max} are given in Table 12 and Fig. 44. In this test, the allowed K_{max} was not exceeded.

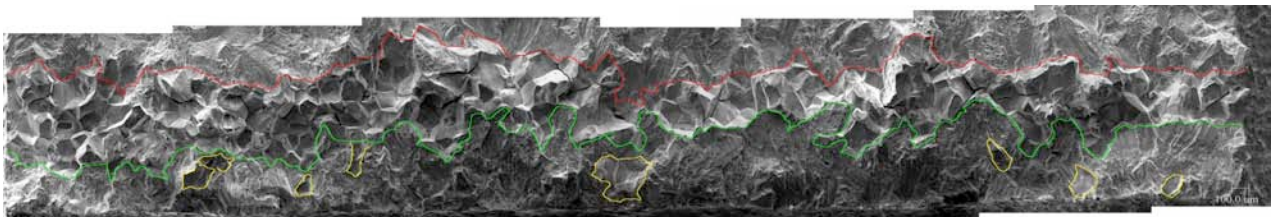


Figure 45. Micrograph of the fracture surface of Specimen N3CC-3. Crack growth is from bottom to top.

Unlike the previous two specimens where an IG fracture mode was observed right from the beginning, this specimen exhibited a TG region at the start of the test; that is, under more rapid cyclic loading, the crack growth is dominated by mechanical fatigue. The CGRs during precracking and initial periods of cyclic loading were primarily due to mechanical fatigue. For the present test, environmental enhancement typically was observed at load ratios $R \geq 0.5$ and rise times ≥ 30 s.

To better illustrate these features, Fig. 46 shows a portion of the fracture surface of the specimen at higher magnification. Figure 46a shows the full extent of the crack, from the machined notch (bottom of the picture) to the end of the test. During precracking, the crack advances in a predominantly TG mode; however, grains appear well-defined and IG cracks are also observed. Moreover, as already indicated, several locations are characterized by smooth IG fracture (indicated by white arrows in

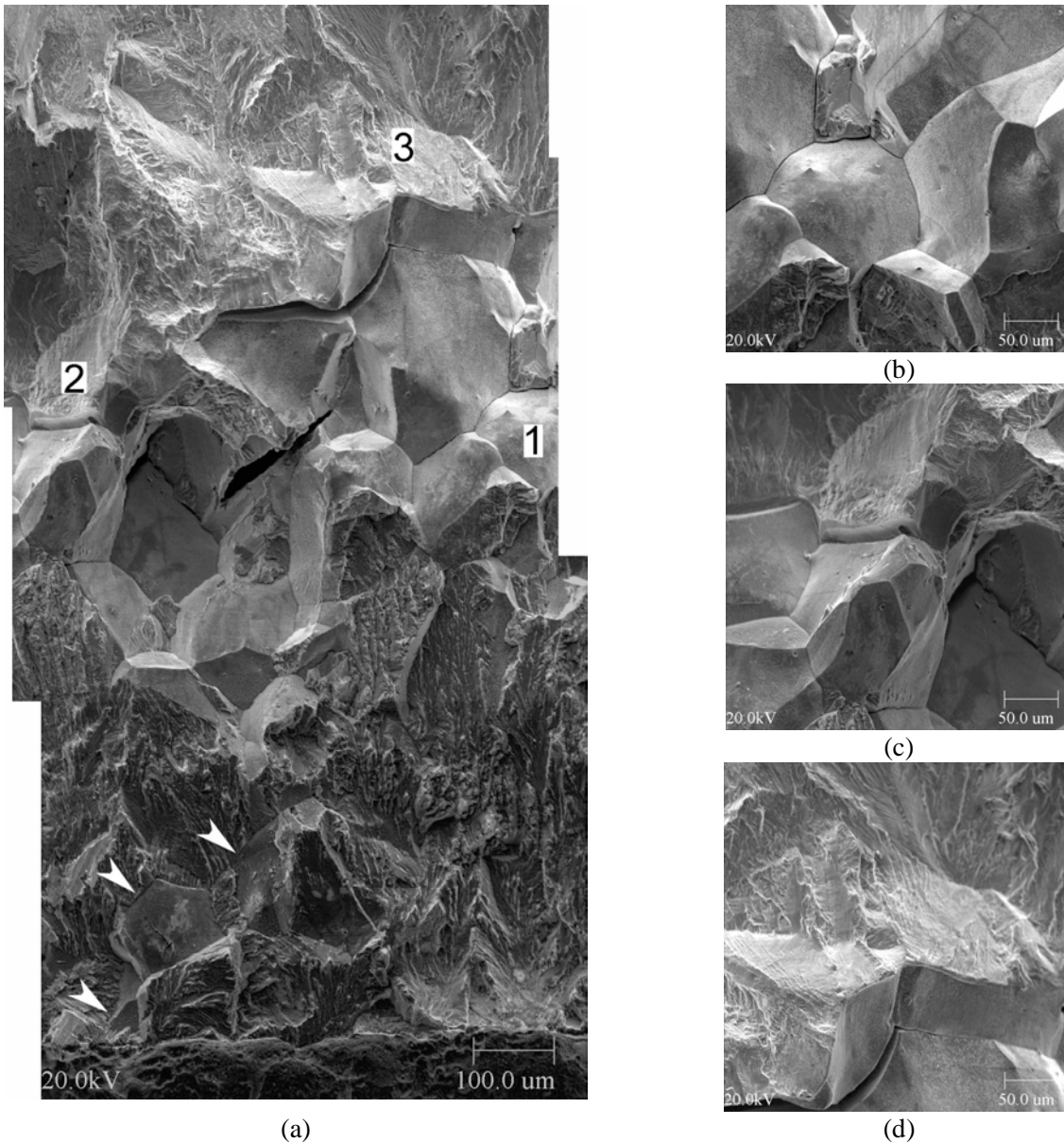


Figure 46. (a) Micrograph showing a portion of the fracture surface of N3CC-3 and high-magnification micrographs at locations (b) 1, (c) 2, and (d) 3. The arrows indicate grains exhibiting smooth IG in the TG region corresponding to the precracking periods.

Fig. 46a). As with the previous specimens, smooth IG fracture was observed right from the beginning of the test in regions corresponding to fatigue cracking. Several high-magnification micrographs taken at locations 1–3 are shown in Figs. 46b–d. Figure 46b (location 1 in Fig. 46a) shows an example of smooth IG fracture from the exclusively IG region corresponding to the constant-load test period. Figure 46c (location 2 in Fig. 46a) shows the fracture surface in a region near the end of the test, and Fig. 46d (location 3 in Fig. 46a) is a micrograph showing the area at the end of the test. One interesting feature of Fig. 46c is that while the last two boundaries encountered by the propagating SCC crack are well-defined, thus likely to crack, the crack follows a TG path in close proximity to the boundary, but not along the boundary.

4.2.2 Davis-Besse J-Groove Weld

Crack growth tests have been conducted on 1/4-T and 1/2-T CT specimens in C orientation (Specimens J11CC-1 and J11CC-3, respectively).

4.2.2.1 Specimen J11CC-1

Fatigue precracking was carried out at $R \approx 0.3$, $K_{\max} \approx 20.0 \text{ MPa}\cdot\text{m}^{1/2}$, and triangular waveform with 1–0.01 Hz frequency. After $\approx 0.18\text{-mm}$ (7 mil) crack extension, R was increased incrementally to 0.7, and the loading waveform changed to a slow/fast sawtooth with rise time of 300 s or 1000 s. The ECPs of the Pt electrode and the companion Alloy 600 electrode located downstream from the autoclave were -648 and -651 mV, respectively. The test conditions, experimental CGRs, the allowed K_{\max} from K/size criterion, and the margin between the applied and allowed K_{\max} are given in Table 13. The changes in crack length and K_{\max} with time during test periods 3–13 are shown in Fig. 47.

Table 13. CGR data for Specimen J11CC-1 of Alloy 182 J-groove weld in PWR water^a at 316°C.

Test Period	Test Time (h)	Conductivity ^b ($\mu\text{S}/\text{cm}$)	R Load Ratio	Rise Time (s)	Down Time (s)	Hold Time (s)	Kmax ($\text{MPa}\cdot\text{m}^{1/2}$)	ΔK ($\text{MPa}\cdot\text{m}^{1/2}$)	Growth Rate, (m/s)	Allowed K_{\max}^c ($\text{MPa}\cdot\text{m}^{1/2}$)	$K_{\text{app}} - K_{\max}^c$ (%)	Crack Length (mm)
Pre a	145	17.2	0.30	0.5	0.5	0	22.5	15.7	4.05E-08	20.9	8	6.153
Pre b	186	17.2	0.31	50	50	0	21.8	15.1	1.27E-09	20.7	5	6.264
1	331	15.6	0.50	300	4	0	21.8	10.9	1.13E-10	20.5	6	6.333
2	453	13.0	0.70	1000	12	0	22.6	6.8	5.71E-12	20.5	10	6.342
3a	644	22.2	0.49	1000	12	0	22.4	11.4	3.88E-11	20.5	9	6.363
3b	745	20.0	0.49	1000	12	0	22.3	11.4	negligible	20.4	9	6.382
4	937	14.7	0.49	1000	12	0	23.8	12.2	8.25E-12	20.4	17	6.392
5	987	14.7	0.49	300	12	0	23.8	12.2	5.53E-11	20.4	17	6.401
6	1106	18.2	0.49	300	12	3600	23.9	12.2	negligible	20.4	17	6.402
7	1178	18.9	0.51	30	4	0	24.2	11.9	7.93E-10	20.4	20	6.525
8	1248	17.2	0.48	300	12	0	24.3	12.6	1.06E-10	20.4	21	6.550
9	1415	16.1	0.74	300	12	3600	24.3	6.4	negligible	20.4	20	6.543
10	1443	18.2	0.48	30	12	0	24.6	12.9	1.13E-09	20.0	23	6.616
11	1513	18.5	0.48	300	12	0	29.0	15.0	3.00E-10	19.8	47	6.742
12	1548	18.5	0.48	300	12	3600	29.3	15.1	4.00E-11 ^d	19.8	48	6.747
13	1948	16.7	1.0	–	–	–	30.3	0.0	1.63E-11 ^e	19.7	54	6.797

^aSimulated PWR water with 2 ppm Li, 1000 ppm B, and ≈ 2 ppm dissolved hydrogen (23 cc/kg).

^bRepresents values in the effluent. Feedwater conductivity was about the same as in the effluent. Effluent DO was <10 ppb.

^cBased on flow stress.

^dFrom superposition model, CGR during the constant load was estimated to be $1.68\text{E-}11$ m/s.

^eBased on total crack extension during the period.

For this specimen, relatively high CGRs were observed under cyclic loading (e.g., $>1 \times 10^{-10}$ m/s), but attempts to transition to constant load by increasing the load ratio and/or rise time, decreased the CGRs to very low levels. As shown in Table 13, during test period 2, the CGR decreased markedly at $R = 0.7$ and a rise time of 1000 s. The CGR also decreased significantly each time a 3600-h hold period

was added to the cycle, e.g., during test periods 6, 9, and 12. Measurable growth rates were observed when K_{max} was increased above $25 \text{ MPa}\cdot\text{m}^{1/2}$ and at $R = 0.5$ and a 300 s rise time. The CGR under the final constant-load test period at $K_{max} \approx 30 \text{ MPa}\cdot\text{m}^{1/2}$ was relatively low.

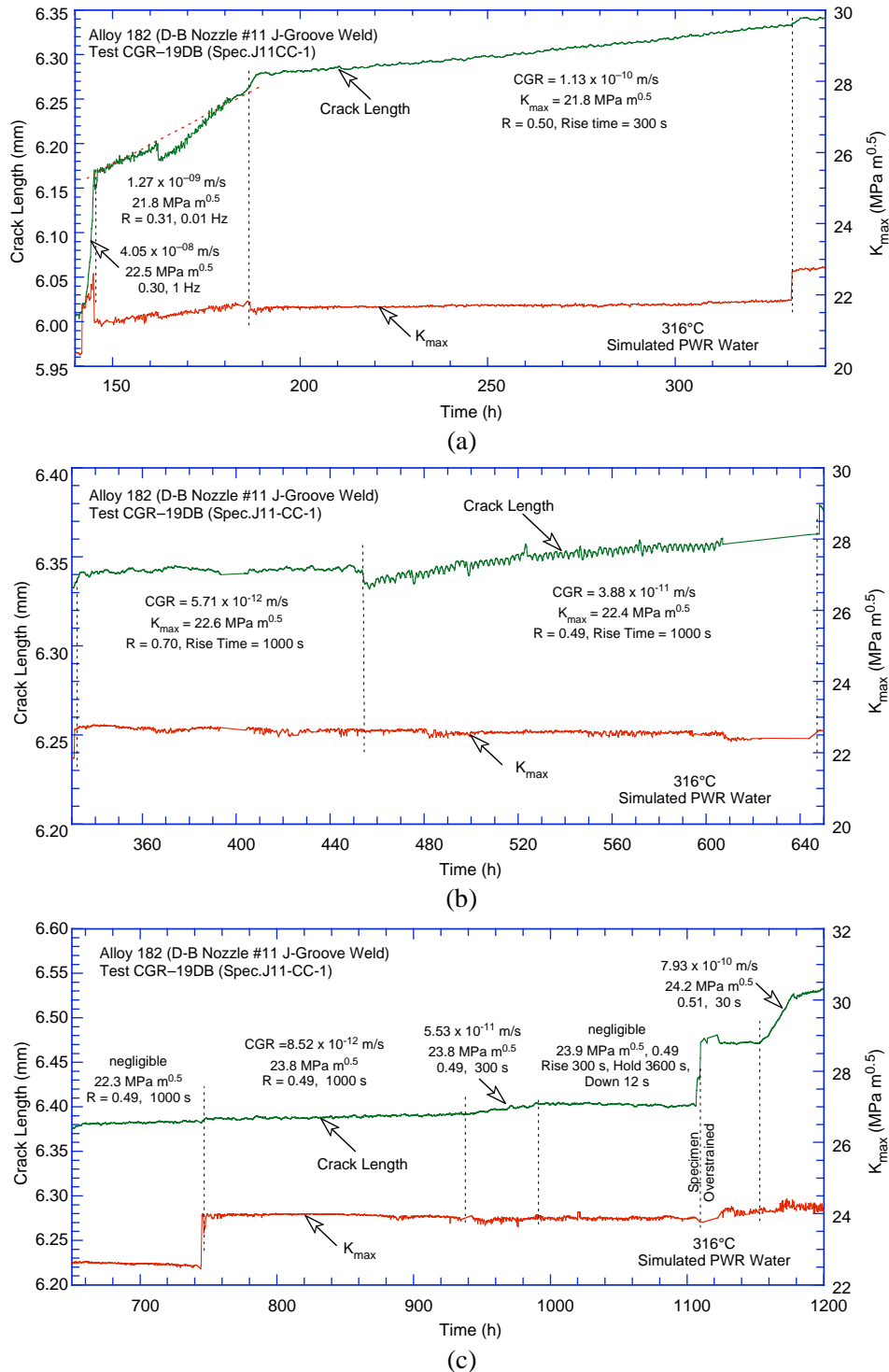


Figure 47. Crack length vs. time plots for Specimen J11CC-1 of Alloy 182 J-groove weld in PWR water at 316°C during test periods (a) precracking, (b) 1–3a, (c) 3b–7, (d) 8–11, and (e) 12–13.

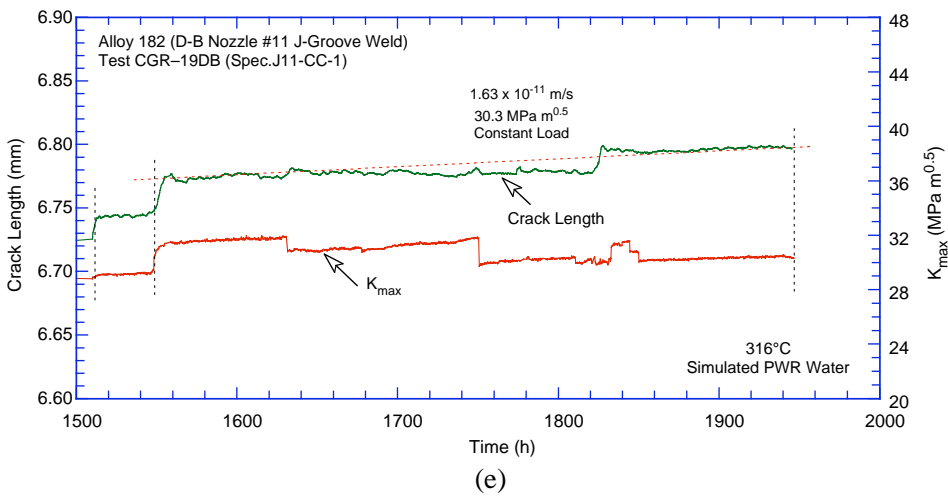
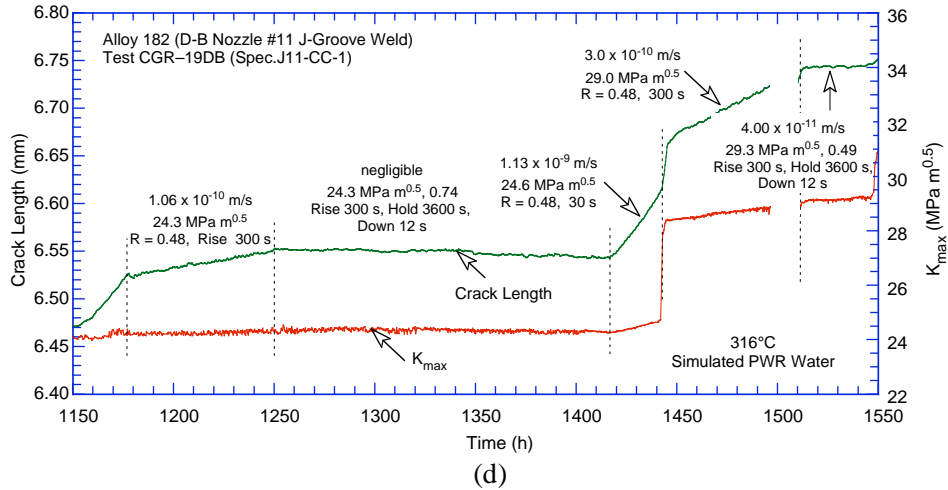


Figure 47. (Contd.)

Figure 48 shows the entire crack extension for the specimen. On the basis of this photograph, the actual crack extension was estimated to be 60% greater than the value determined from the DC potential drop method; the values shown in Table 13 and Fig. 47 have been corrected accordingly.

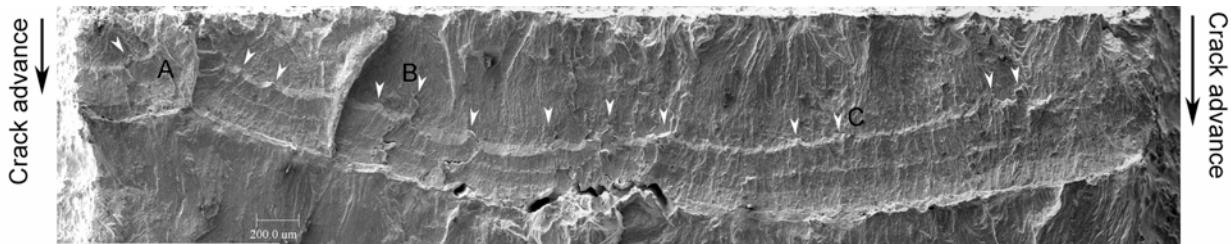


Figure 48. Crack front on Sample J11CC-1. Crack growth is from top to bottom.

Figure 48 shows that after precracking, the fracture turned into a mixed transgranular and IG fracture mode. While it appears that TG fracture is the dominant mode overall, the area near the left edge contains more IG fracture than the average. The crack also appears to be pinned on the left side on the photo, most likely by a material defect. Furthermore, the appearance of the crack front suggests that pinning occurred throughout the fracture surface, thereby impeding the crack advance. Several locations where pinning was evident are indicated by arrows in Fig. 48.

A detailed examination at high magnification was conducted at three locations on the fracture surface, designated by A, B, and C in Fig. 48. Figure 49 shows an example of crack morphology at position A. Figures 49a and 49b are examples of mixed TG and IG fracture. The secondary cracks visible in Fig. 49b are consistent with an IG fracture mode. Figure 49c is a high-magnification micrograph taken at what appears to be a pinning point. The presence of striations (top center) suggests a TG fracture mode. These two observations suggest that the SCC-driven, IG-propagating crack was stopped at obstacles. The crack front apparently overcame the obstacles only after the loading conditions were changed to promote mechanical fatigue.

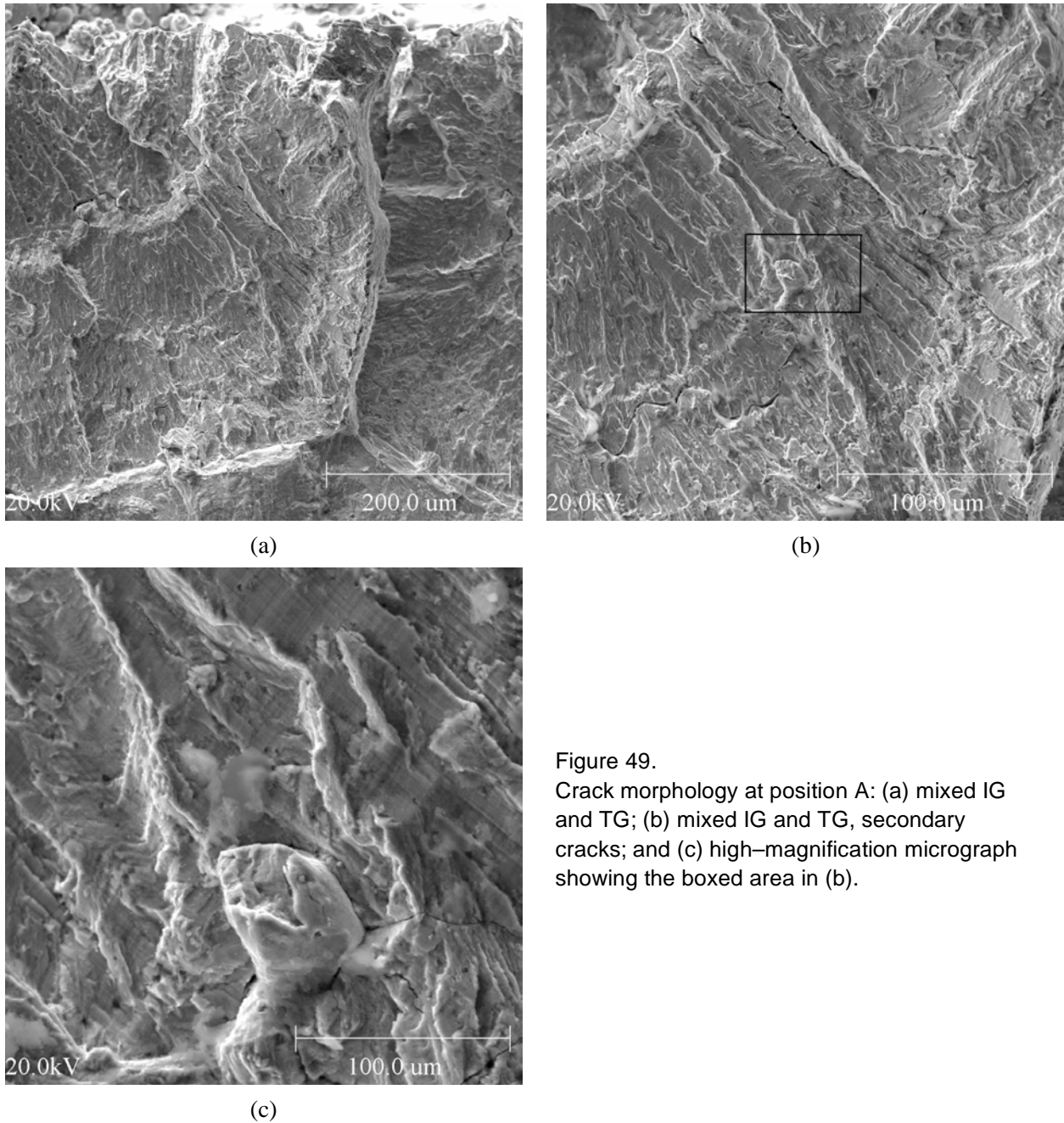


Figure 49.
Crack morphology at position A: (a) mixed IG and TG; (b) mixed IG and TG, secondary cracks; and (c) high-magnification micrograph showing the boxed area in (b).

Figure 50 shows the crack morphology at position B in Fig 48. Figures 50a and b are examples of mixed IG and TG, and Figs. 50c and d are high-magnification micrographs at locations indicated by arrows in Fig. 50a. The upper right-hand corner of Fig. 50c shows a relatively smooth surface, while Fig. 50d shows rounded shapes typical of dendritic undulations, both cases typical of SCC-driven crack advance. The crack growth was apparently interrupted by pinning points, two of which are visible in Fig. 50c. Out-of-plane cracks are also apparent in Figs. 50c and d. While these may be preexisting cracks, none were observed during metallography. More likely, they formed during the test at either the advancing crack tip or after the crack tip has passed. Since these cracks seem to follow the pinning pattern of the fracture surface, the first hypothesis – crack branching at the crack tip – seems more probable. The root cause for the occurrence of these cracks is unknown.

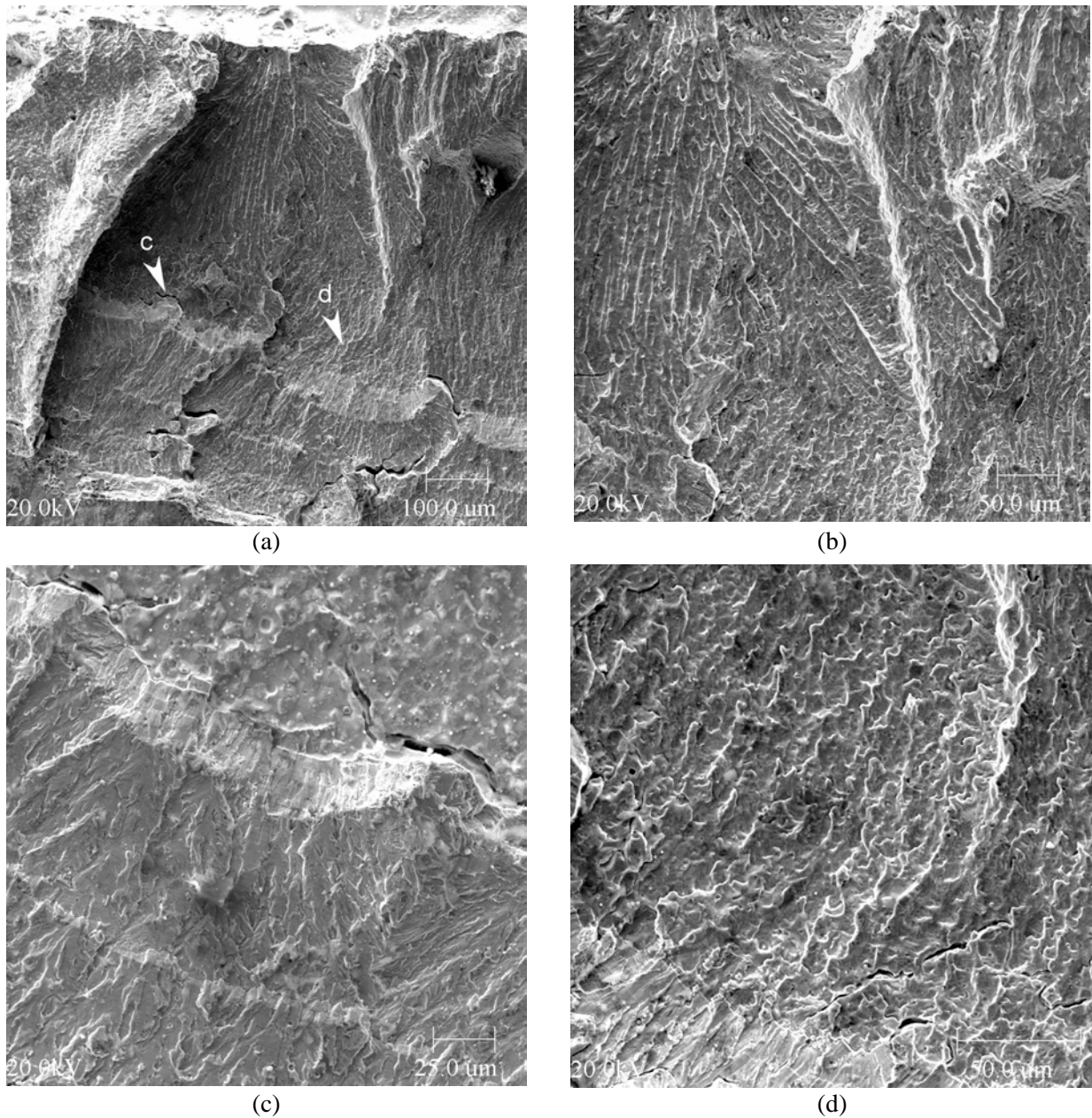


Figure 50. Crack morphology at position B: (a, b) mixed IG and TG, and (c, d) high-magnification micrographs at locations indicated by arrows in (a).

Figure 51 further substantiates the observations just made. Figure 51a shows the crack morphology at position C in Fig 48. Figure 51b shows a mixed IG/TG mode. The striations on the fracture surface past the pinning point, Fig. 51c, seem to indicate that the SCC-driven crack was pinned and unable to advance unless fatigue driven. Out-of-plane cracks were also observed, as indicated in Fig. 51b.

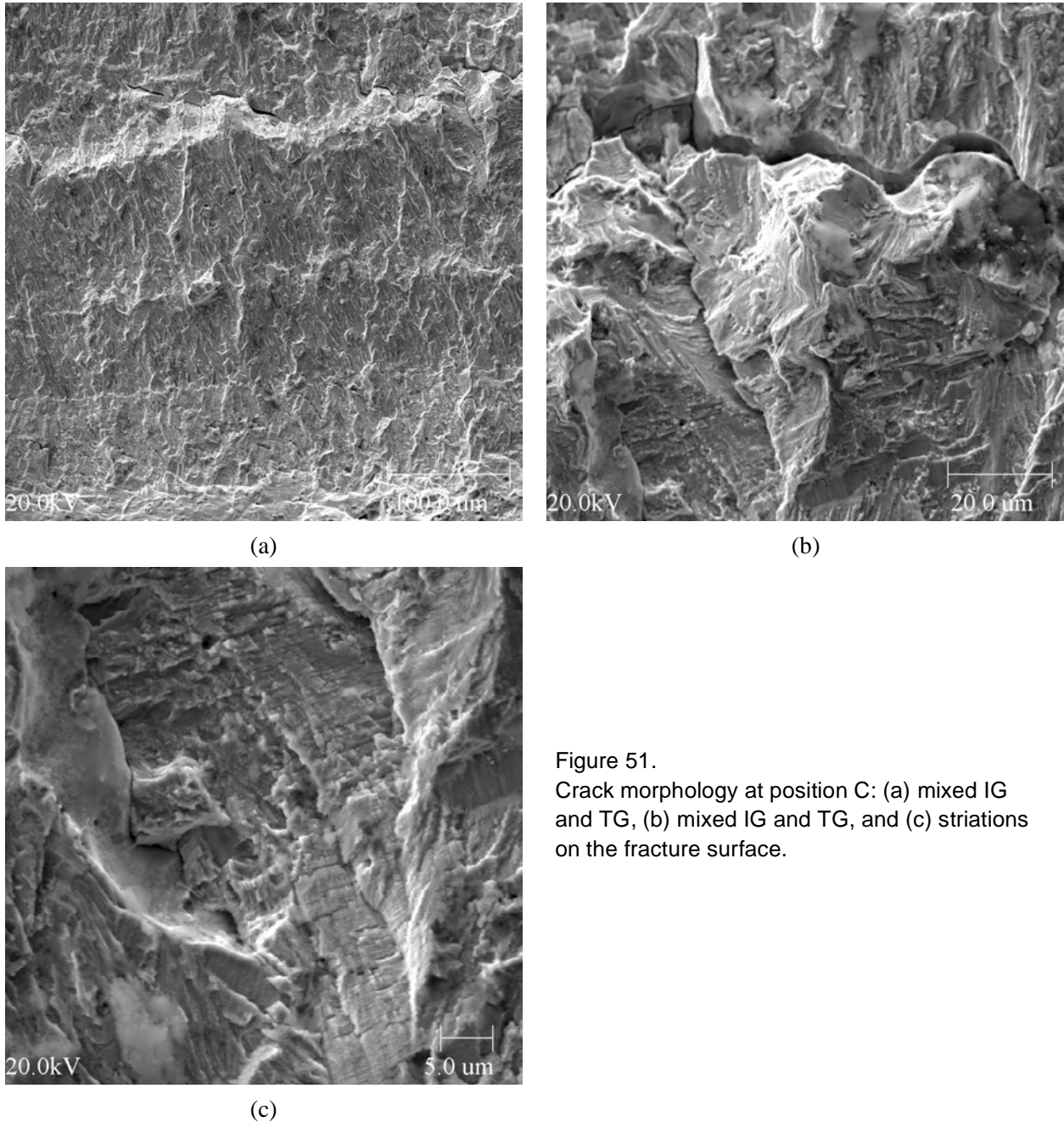


Figure 51.
Crack morphology at position C: (a) mixed IG and TG, (b) mixed IG and TG, and (c) striations on the fracture surface.

4.2.2.2 Specimen J11CC-3

Testing for this specimen was similar to that of the previous Alloy 182 specimen from the Davis-Besse CRDM nozzle J-groove weld. However, Specimen J11CC-3 was a 1/2-T CT specimen. Fatigue precracking was carried out at $R \approx 0.3$, $K_{\max} \approx 18.0 \text{ MPa}\cdot\text{m}^{1/2}$, and triangular waveform with 0.5–0.01 Hz

frequency. Next, R was increased incrementally to 0.7, and the loading waveform changed to a slow/fast sawtooth with rise time of 300 s or 1000 s. The test conditions, experimental CGRs, the allowed K_{max} from K/size criterion, and the margin between the applied and allowed K_{max} are given in Table 14. The changes in crack length and K_{max} with time are shown in Fig. 52.

A significant result for this specimen is the very low CGRs under constant load, with or without periodic partial unloading. Also, every time the loading was changed from a sawtooth waveform to constant load, the crack length estimated from the DC potential measurements decreased by $\approx 20 \mu\text{m}$, as indicated by Fig. 52. Our experience to date has been that the DC potential drop method measures crack length accurately when the fracture morphology is TG, but when the fracture mode is IG, the potential drop underestimated the actual crack length, most likely because of the presence of unbroken ligaments or secondary cracks. In an attempt to obtain more consistent crack-length measurements by DC potential drop, the specimen was subjected to short periods of cyclic loading with a sawtooth waveform at $R = 0.5$ or 0.7 and a 300– or 1000–s rise time before and after each constant load test period, e.g., test periods 7, 9, and 13. The average crack length during these short test periods was used to determine the CGRs for the constant-load test periods; the values are given in Table 14.

Table 14. CGR data for Specimen J11CC-3 in PWR water^a at 316°C.

Test Period	Test Time (h)	Conductivity ^b ($\mu\text{S}/\text{cm}$)	R Load Ratio	Rise Time (s)	Down Time (s)	Hold Time (s)	K_{max} ($\text{MPa}\cdot\text{m}^{1/2}$)	ΔK ($\text{MPa}\cdot\text{m}^{1/2}$)	Growth Rate (m/s)	Allowed K_{max} ($\text{MPa}\cdot\text{m}^{1/2}$)	$K_{app} - K_{max}^c$ (%)	Crack Length (mm)
Pre a	78	21	0.31	0.25	0.25	0	18.78	13.17	6.55E-08	29.40	-36	12.373
Pre b	104	21	0.32	10	10	0	18.96	13.02	7.17E-09	29.10	-35	12.605
1	221	18	0.50	60	4	0	19.81	9.94	7.44E-10	28.53	-31	13.049
2	412	20	0.51	300	12	0	19.95	9.97	1.33E-10	28.42	-30	13.134
3	507	20	1.00	–	–	–	19.99	0.00	3.92E-11 ^d	28.47	-30	13.157
4	580	19	0.50	300	12	0	22.08	11.10	2.30E-10	28.29	-22	13.233
5	742	15	0.50	1000	12	0	22.21	11.13	7.12E-11	28.27	-21	13.254
6a	864	13	1.00	–	–	–	22.23	0.00	–	28.33	-22	13.246
6b	934	13	0.51	12	12	3600	22.16	11.07	3.93E-11 ^d	28.33	-22	13.282
7b	941	19	0.70	1000	12	0	28.11	8.45	–	28.21	0	–
8	1079	33	0.70	12	12	3600	28.18	8.46	4.00E-11	28.24	0	13.271
9	1084	33	0.70	1000	12	0	28.36	14.41	–	28.19	1	13.312
10	1248	31	0.70	12	12	3600	32.72	9.82	4.65E-11	28.17	16	13.327
11	1349	29	0.69	1000	12	0	32.80	10.04	8.23E-11	28.06	17	13.410
12	1516	28	0.70	12	12	3600	32.60	9.78	negligible	28.12	16	13.368
13	1537	28	0.70	300	12	0	32.74	9.82	–	28.07	17	13.405

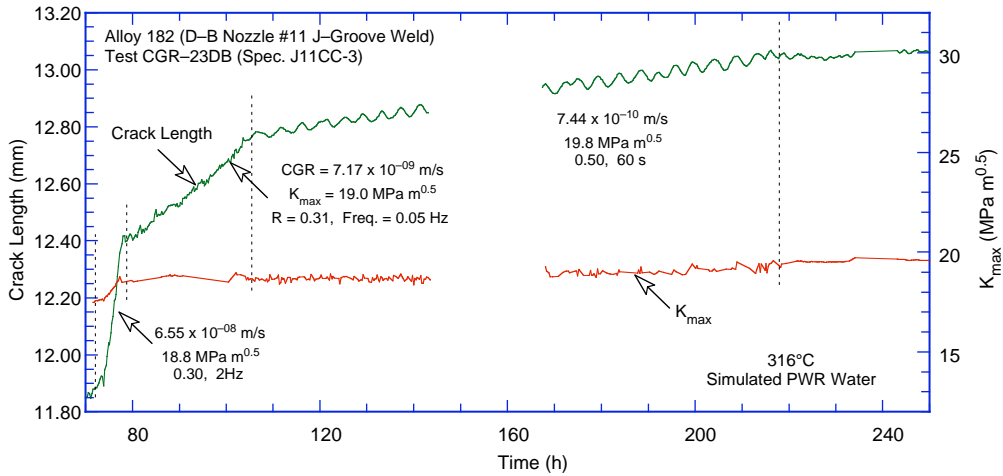
^aSimulated PWR water with 2 ppm Li, 1000 ppm B, and ≈ 2 ppm dissolved hydrogen. Effluent DO was < 10 ppb.

^bRepresents values in the effluent; ECP measurements were not made because of problems with the reference electrode. Feedwater conductivity was about the same as in the effluent.

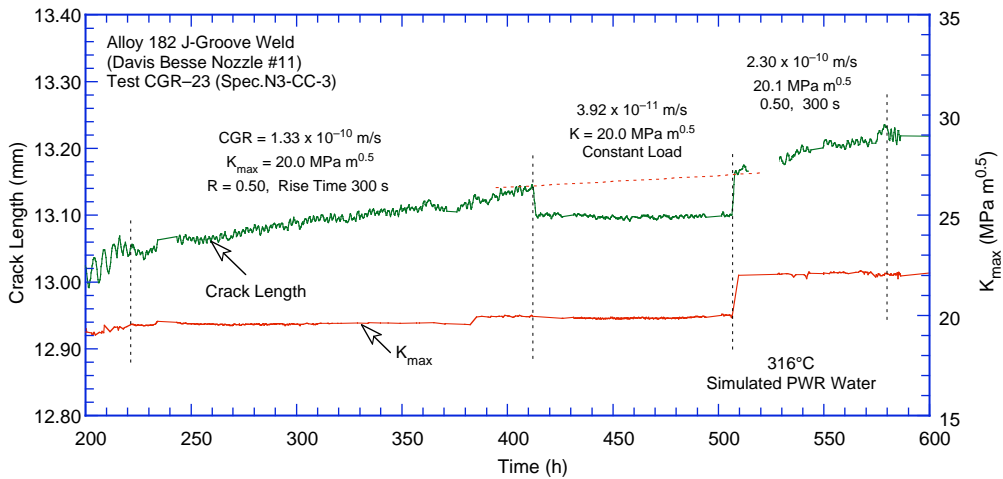
^cBased on flow stress.

^dValues estimated from the total crack extension during the test period and not from the slope of the crack length vs. time plot.

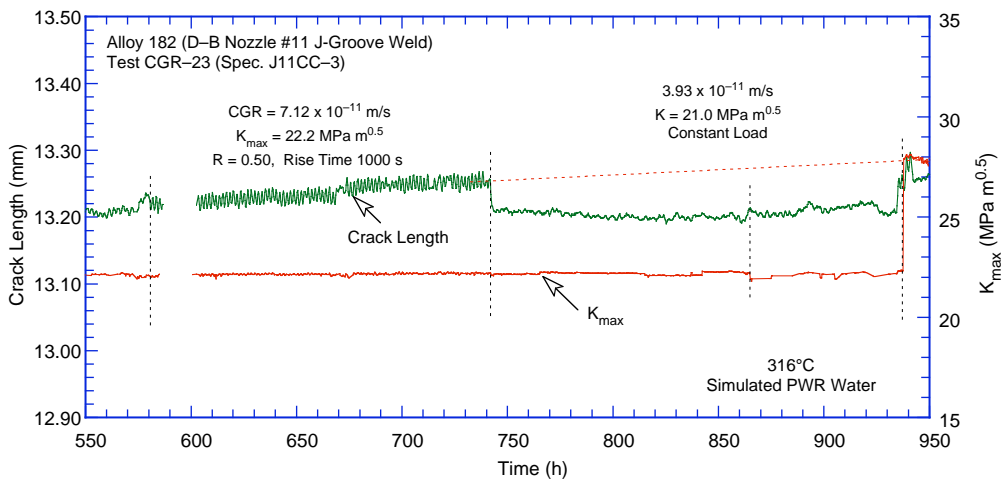
A detailed metallographic evaluation of the specimen was performed to verify the crack length measurements and to characterize the fracture morphology. Composite micrographs of the cross section and the fracture surface are shown in Figs. 53 and 54, respectively. The beach mark on the fracture surface just below the region marked #3 in Fig. 54 and extending across the width of the specimen corresponds to the end of test period 1. Fracture occurred along the plane perpendicular to the stress axis up to the beach mark, Fig. 53, and away from this plane for other test periods. Also, the fracture morphology up to the beach mark is predominantly TG, whereas some regions of IG fracture are observed in test periods with long rise times or long hold periods.



(a)



(b)



(c)

Figure 52. Crack length vs. time plots for Specimen J11CC-3 of Alloy 182 in PWR water at 316°C during (a) precracking and test period 1, (b) 2–4, (c) 5–7, and (d) 8–13.

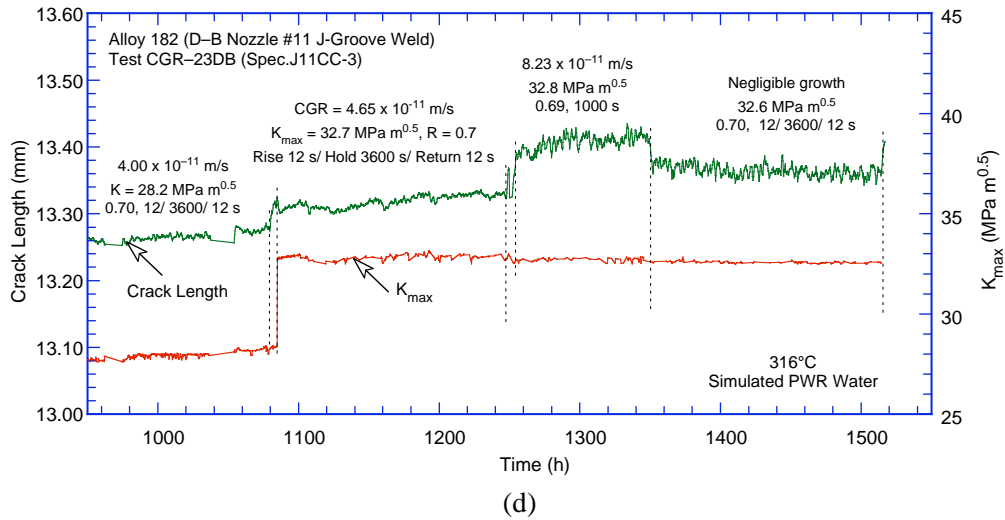


Figure 52. (Contd.)

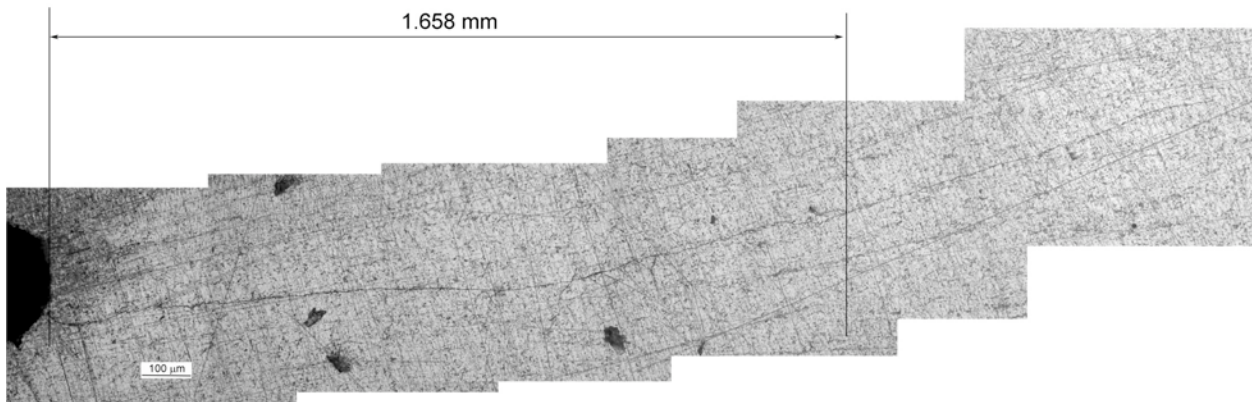


Figure 53. Micrograph of the cross section of Specimen J11CC-3 showing the fracture-plane profile.

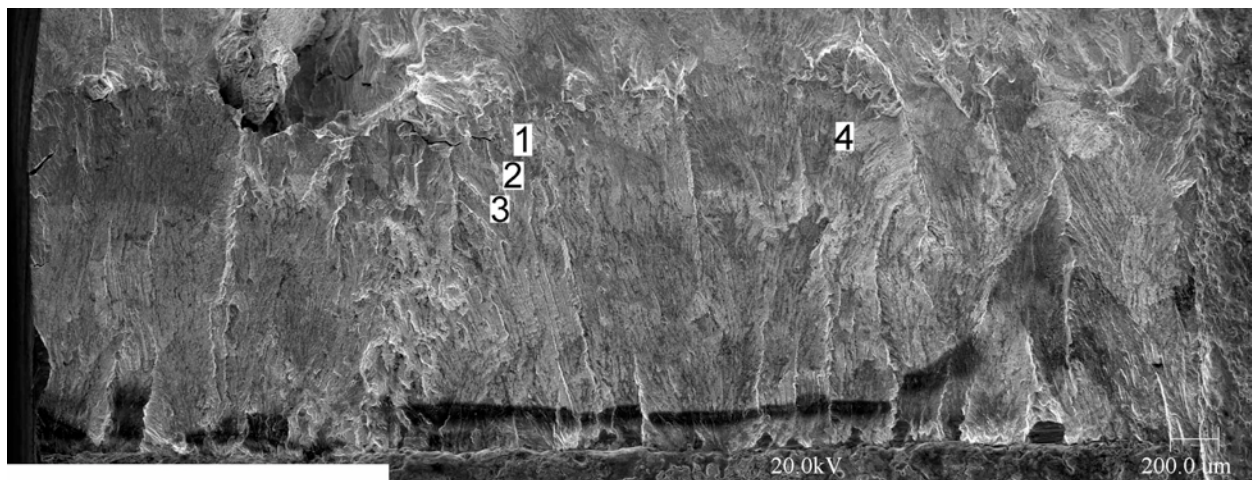


Figure 54. Micrograph of the fracture surface of Specimen J11CC-3 tested in PWR water at 316°C.

The final crack length was measured from the SEM micrograph. The actual crack length was a factor of ≈ 2 greater than the value determined from the DC potential measurements. The experimental crack extensions were scaled proportionately. The corrected CGRs are given in Table 14.

The entire crack extension in the region marked #4 in Fig. 54 is shown in Fig. 55. The fracture mode is predominantly TG; some regions of IG fracture are observed in the final $\approx 200\text{-}\mu\text{m}$ crack extension (i.e., test periods 6–13). Several ridges, parallel to the direction of crack extension, are observed in the predominantly TG region of the fracture surface (i.e., test periods 1–3). As seen before in Specimen J11CC-1, the fracture surface obtained under cyclic loading with a long rise time or constant load with or without periodic unloading (test periods 5–13) shows several out-of-plane cracks suggesting crack branching at the crack tip (e.g., Fig. 56). These out-of-plane cracks may be responsible for the low growth rates observed for the material.

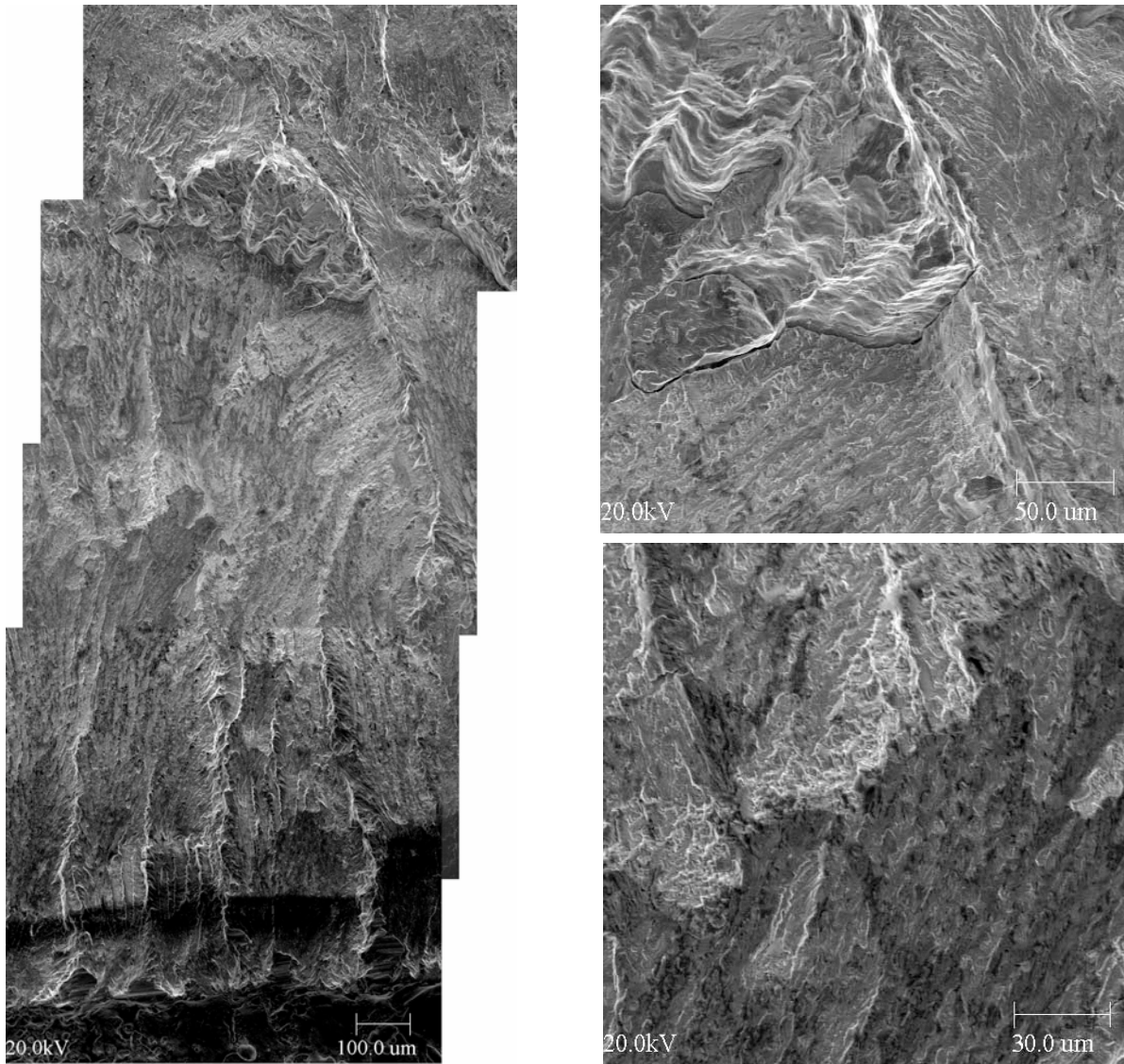


Figure 55. Micrographs showing a slice of the entire length of the fracture surface and high-magnification micrographs of the surface at select locations.

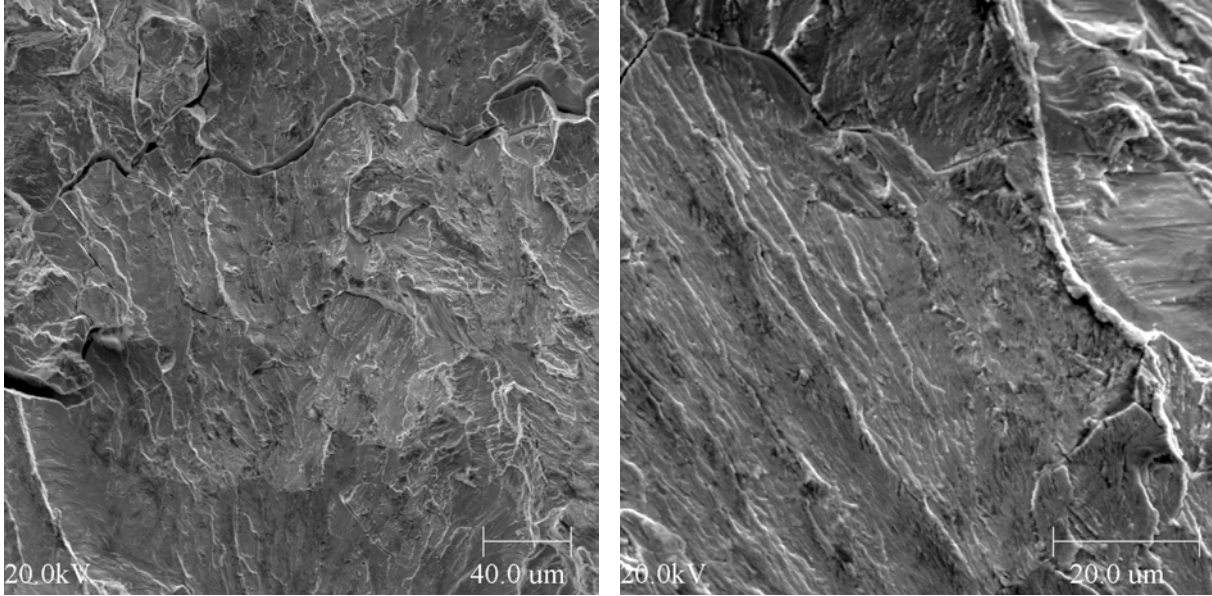


Figure 56. Micrographs showing IG secondary cracks parallel to the crack front in Specimen J11CC-3 tested in PWR water at 316°C.

4.2.3 V.C. Summer Nozzle-to-Pipe Weld

4.2.3.1 Specimen WCR-01

The first weld specimen from V.C. Summer material, made of Alloy 82, was tested in a simulated primary water environment at 320°C. Fatigue precracking was carried out at $K_{max} \approx 24.0 \text{ MPa}\cdot\text{m}^{1/2}$, $R \approx 0.3$, and triangular waveform with 0.5–0.1 Hz frequency. Next, R was increased incrementally to 0.5, and the loading waveform was changed to a slow/fast sawtooth with a rise time of 30 or 300 s. The crack growth data along with the test conditions, resulting stress intensity factors K_{max} , and experimental and estimated CGRs for the two specimens are given in Table 15 and Fig. 57. For this specimen, testing concluded with a constant-load period at $K_{max} = 24.2 \text{ MPa}\cdot\text{m}^{1/2}$.

Table 15. CGR data for Specimen WCR-01 of the Alloy 82 SMA weld in PWR water^a at 320°C.

Test Period	Test Time (h)	Conductivity ^b (μS/cm)	O ₂ Conc. ^b (ppb)	Load Ratio R	Rise Time (s)	Down Time (s)	Hold Time (s)	K _{max} ^c (MPa·m ^{1/2})	ΔK (MPa·m ^{1/2})	CGR _{env} (m/s)	Est'd. A182 CGR _{air} ^d (m/s)	Crack Length (mm)
Pre a	100	23	<10	0.32	1	1	0	24.14	16.42	2.83E-09	5.20E-08	12.289
Pre b	124	23	<10	0.31	0.5	0.5	0	24.14	16.66	4.86E-09	1.08E-07	12.351
Pre c	140	23	<10	0.29	5	5	0	23.18	16.46	1.72E-09	9.77E-09	12.379
Pre d	146	23	<10	0.30	0.25	0.25	0	23.96	16.77	9.34E-09	2.16E-07	12.484
1	258	23	<10	0.30	30	2	0	24.35	12.17	1.39E-10	7.99E-10	12.649
2	380	23	<10	0.52	30	2	0	25.17	12.08	2.06E-10	7.05E-10	12.736
3	523	23	<10	0.50	300	12	0	23.69	11.88	3.18E-11	7.52E-11	12.779
4	593	23	<10	1.00	–	–	–	24.22	0.00	4.11E-11	–	12.789

^aSimulated PWR water with 2 ppm Li, 1100 ppm B, and 2 ppm dissolved hydrogen (≈23 cc/kg). Measured pH was 6.4.

^bRepresents values in the effluent. Feedwater conductivity was about the same as in the effluent.

^cAt the end of the test the maximum allowed K_{max} based on the final load and using Eqn. 11 was $28.8 \text{ MPa}\cdot\text{m}^{1/2}$.

^dCrack growth rates for Alloy 182 weld metal in air determined by Eq. 14 in Section 5.1.

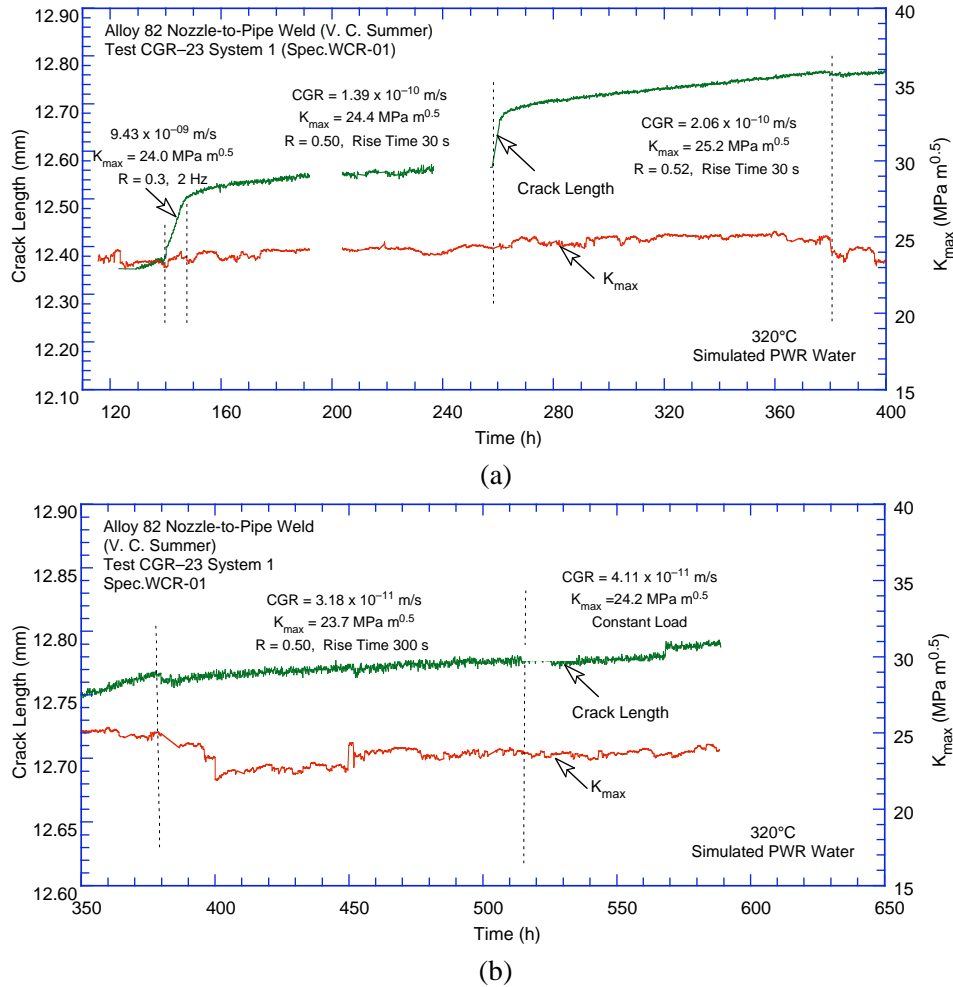


Figure 57. Crack length vs. time for Alloy 82 nozzle-to-pipe weld specimen (V.C. Summer) in simulated PWR environment at 320°C during test periods (a) Pre-crack-2 and (b) 3-4.

The final crack lengths were determined from metallographic examination of the fractured specimens by SEM. The entire fracture surface of WCR-01 is shown in Fig. 58. The first (green) line designates the region where IG features start to be observed, and the second (red) line shows the final crack extension. While a relatively straight crack front is observed, the appearance suggests pinning. Nevertheless, the observed features are consistent with the testing parameters. These features can be better seen in the higher magnification micrographs of Fig. 59. Figure 59a corresponds to the boxed area of Fig. 58. A mixture of TG and IG growth is observed during precracking and cyclic loading (Fig. 59a) and a predominantly IG growth during the final constant-load test (Fig. 59b).

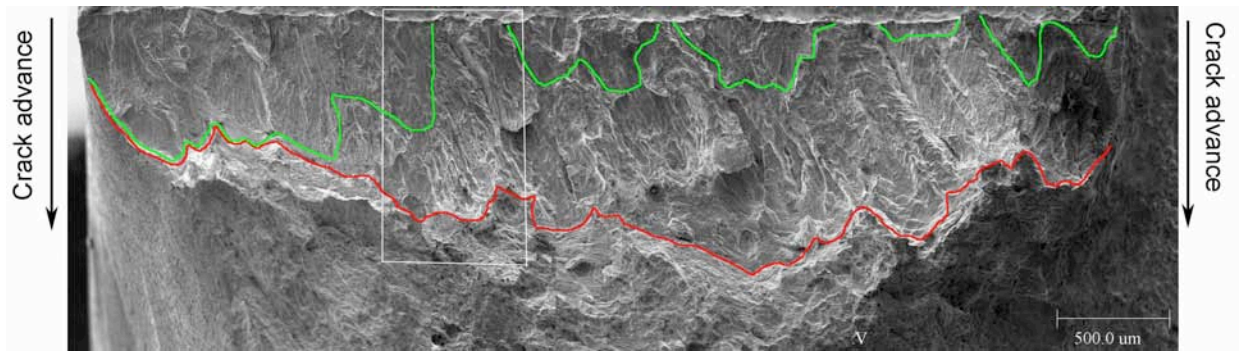


Figure 58. Micrograph of the fracture surface of Specimen WCR-01. Crack advance is from top to bottom.

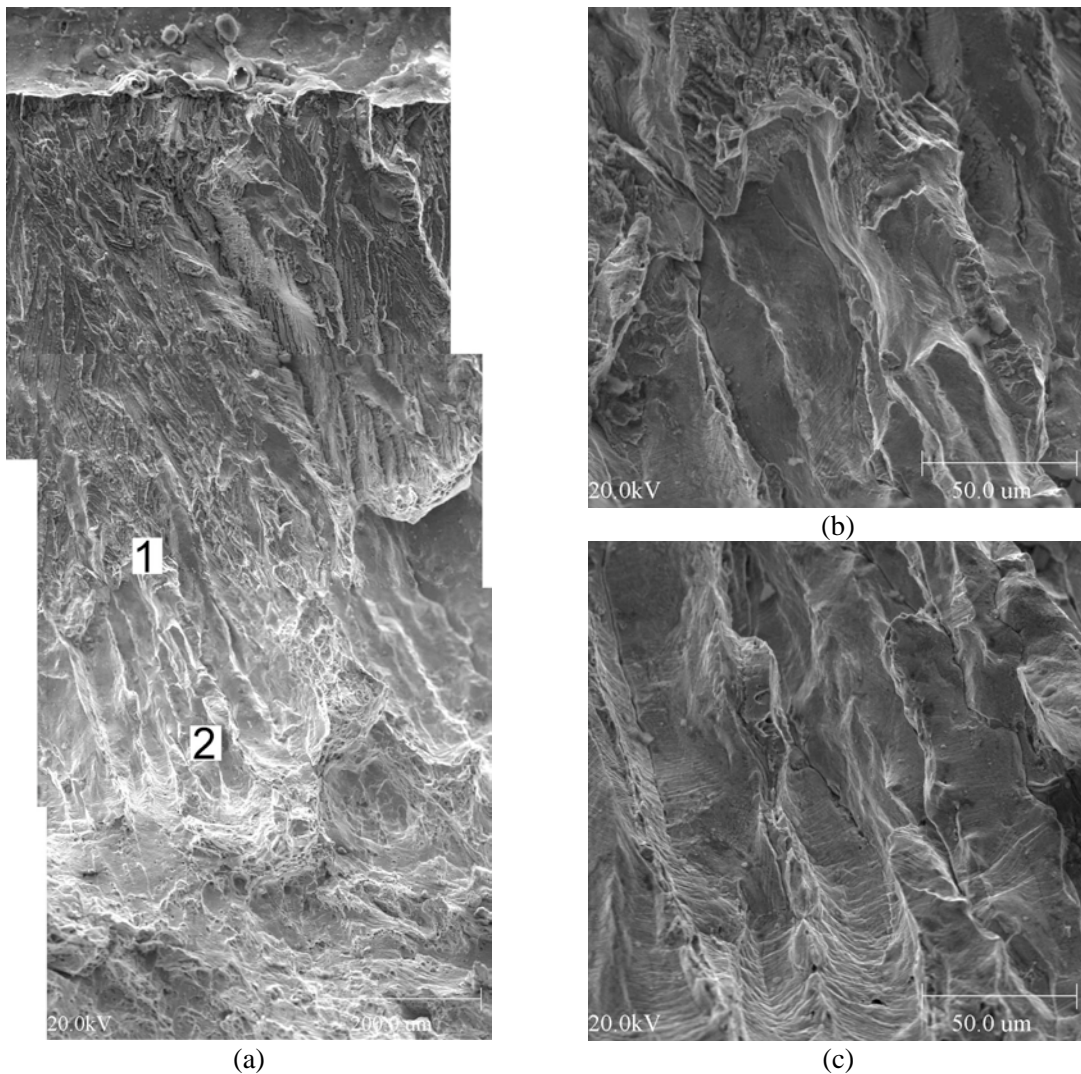


Figure 59. Micrographs of (a) portion of the fracture surface of Specimen WCR-01 (crack advance is from top to bottom), and higher magnification of (b) position 1 and (c) position 2.

On the basis of the image shown in Fig. 59, the crack extension for the entire test was measured to be 0.782 mm (0.031 in.), 2.6 times larger than the value obtained from DC potential measurements.

Especially during IG cracking, it is likely that the two separating surfaces partially touch each other, thus causing the DC potential measurements to underestimate the crack length. Since IG features appeared on the fracture surfaces starting from the early stages of testing, we corrected all crack results, including precracking, by a factor of 2.6. The data shown in Table 15 have been corrected accordingly.

4.2.3.2 Specimen BCR-01

Another test was conducted on the Alloy 182 butter specimen (BCR-01) in a simulated PWR water environment at 320°C. The specimen was fatigue precracked at $K_{\max} = 21 \text{ MPa}\cdot\text{m}^{1/2}$, $R = 0.3$, and a triangular waveform. The specimen was then set at constant load at $K_{\max} = 22.1 \text{ MPa}\cdot\text{m}^{1/2}$ for approximately 300 h. Next, the specimen was cycled at $R = 0.5$ at increasing rise times and set again at constant load at $K_{\max} = 27.0 \text{ MPa}\cdot\text{m}^{1/2}$. Subsequently, the specimen was cycled at $R = 0.5$ at increasing rise times, and set at constant load of $K_{\max} = 32.1 \text{ MPa}\cdot\text{m}^{1/2}$. Following that, the specimen was cycled with the goal of reaching approximately $K_{\max} = 36 \text{ MPa}\cdot\text{m}^{1/2}$, and set at constant load for the final test period. The experimental conditions and results are shown in Table 16, and the changes in crack length and K_{\max} with time are shown in Fig. 60. The ECPs of a Pt electrode and a companion Alloy 600 electrode downstream from the autoclave were -620 and -650 mV (SHE), respectively. For this specimen, the test protocol consisted of four constant-load periods at K_{\max} values up to $36 \text{ MPa}\cdot\text{m}^{1/2}$.

Table 16. CGR data for Specimen BCR-01 of the Alloy 182 SMA weld in PWR water^a at 320°C.

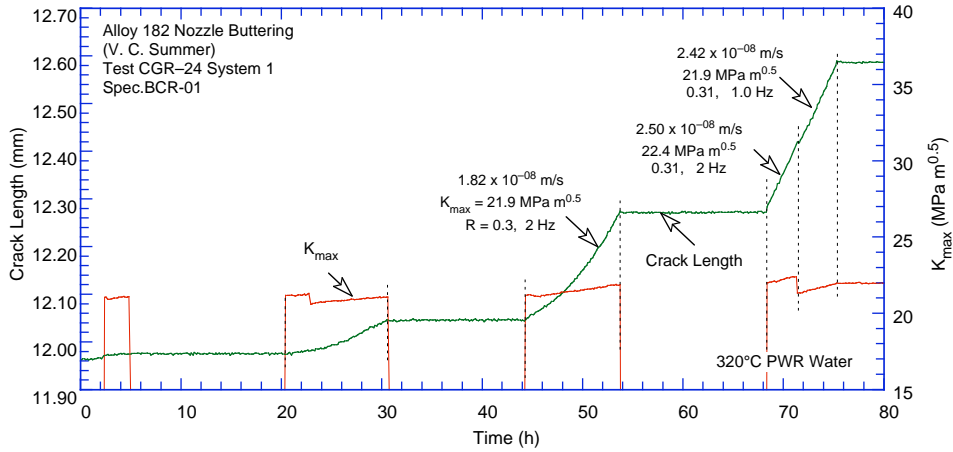
Test Period	Test Time (h)	Conductivity ^b ($\mu\text{S}/\text{cm}$)	O ₂ Conc. ^b (ppb)	Load Ratio R	Rise Time (s)	Down Time, (s)	Hold Time (s)	K_{\max}^c ($\text{MPa}\cdot\text{m}^{1/2}$)	ΔK ($\text{MPa}\cdot\text{m}^{1/2}$)	CGR_{env} (m/s)	Std. A182 $\text{CGR}_{\text{air}}^d$ (m/s)	Crack Length (mm)
Pre a	31.0	26	<10	0.30	0.25	0.25	0	21.07	14.75	4.00E-09	1.28E-07	12.046
Pre b	54.0	26	<10	0.30	0.25	0.25	0	21.91	15.34	1.82E-08	1.50E-07	12.269
Pre c	71.0	26	<10	0.31	0.25	0.25	0	22.42	15.47	2.50E-08	1.59E-07	12.407
Pre d	75.0	26	<10	0.31	0.25	0.25	0	21.91	15.12	2.42E-08	7.24E-08	12.573
1	386.0	26	<10	1.00	–	–	–	22.06	0.00	2.35E-11	–!	12.616
2a	389.0	26	<10	0.50	0.25	0.25	0	25.63	12.82	1.49E-08	1.23E-07	12.715
2b	413.0	26	<10	0.50	0.25	0.25	0	25.81	12.91	1.25E-08	1.27E-07	12.905
3	507.0	26	<10	0.50	50	2	0	26.73	13.36	3.16E-10	7.31E-10	13.041
4	839.0	26	<10	1.00	–	–	–	26.97	0.00	2.34E-11	–	13.057
5	842.0	26	<10	0.30	1	1	0	29.67	20.77	5.04E-08	1.30E-07	13.291
6a	845.0	26	<10	0.50	1	1	0	29.60	14.80	8.18E-09	5.55E-08	13.369
6b	869.0	26	<10	0.50	1	1	0	30.44	15.22	9.17E-09	6.23E-08	13.514
7	939.0	26	<10	0.50	300	12	0	30.60	15.30	2.79E-10	2.12E-10	13.569
8	1,340.0	26	<10	1.00	–	–	–	32.14	0.00	4.49E-11	–	13.594
9	1,343.0	26	<10	0.30	1	1	0	35.05	24.53	5.73E-08	2.57E-07	13.791
10	1344.0	26	<10	0.50	1	1	0	35.70	17.85	1.44E-08	1.20E-07	13.869
11	1346.0	26	<10	0.50	300	12	0	35.21	17.61	5.78E-10	3.77E-10	13.901
12	1702.0	26	<10	1.00	–	–	–	36.03	0.00	4.14E-11	–	13.930

^aSimulated PWR water with 2 ppm Li, 1100 ppm B, and 2 ppm dissolved hydrogen ($\approx 23 \text{ cc}/\text{kg}$). Measured pH was 6.4.

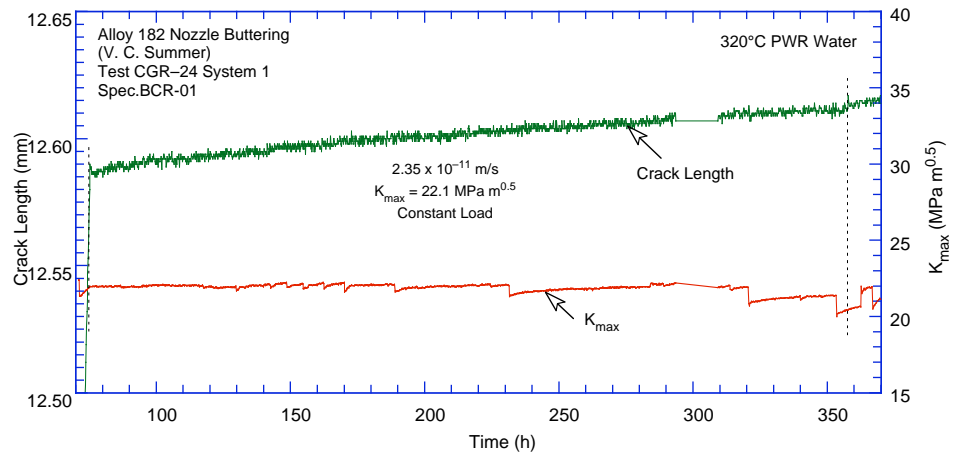
^bRepresents values in the effluent. Feedwater conductivity was about the same as in the effluent.

^cAt the end of the test, the maximum allowed K_{\max} was $26.8 \text{ MPa}\cdot\text{m}^{1/2}$.

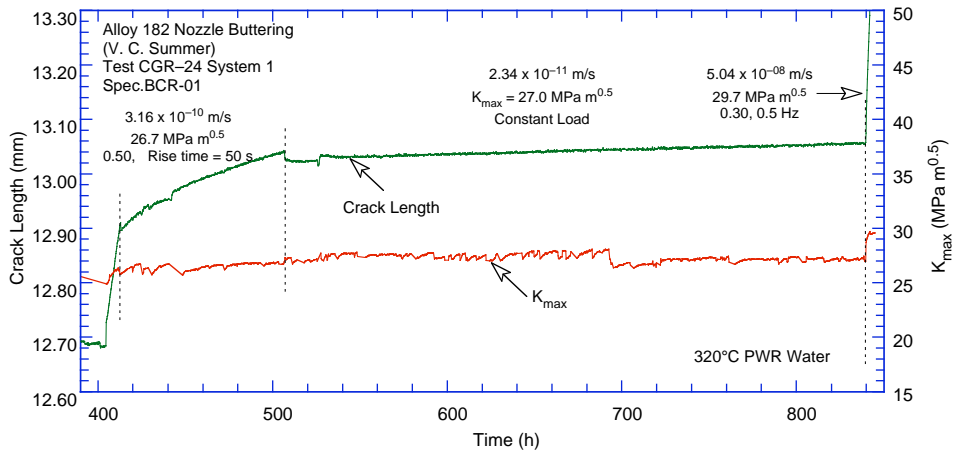
^dCrack growth rates for Alloy 182 weld metal in air determined by Eq. 14 in Section 5.1.



(a)

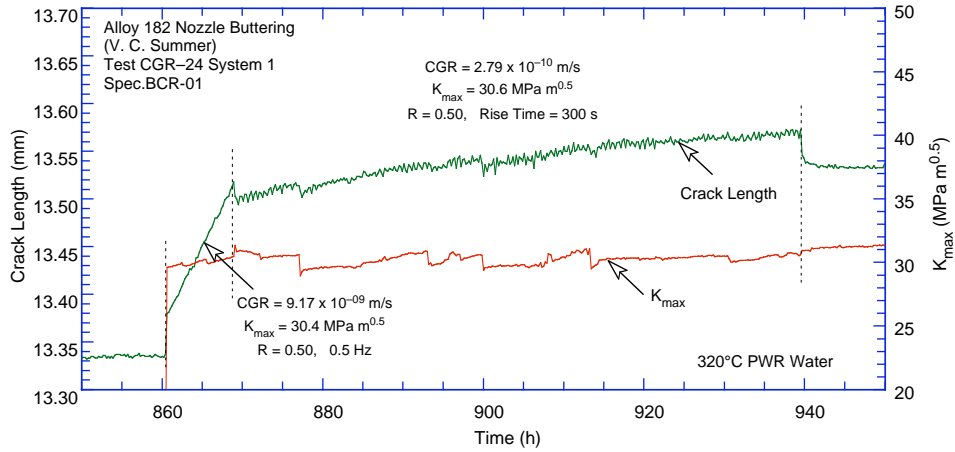


(b)

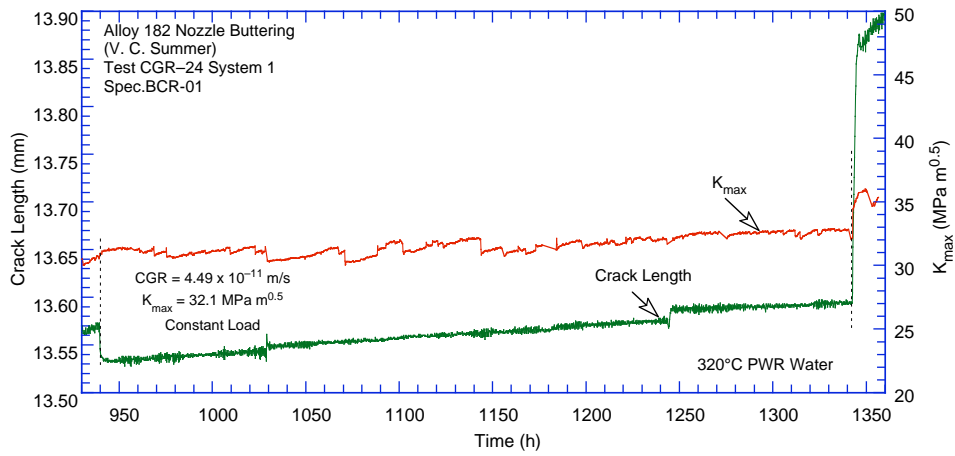


(c)

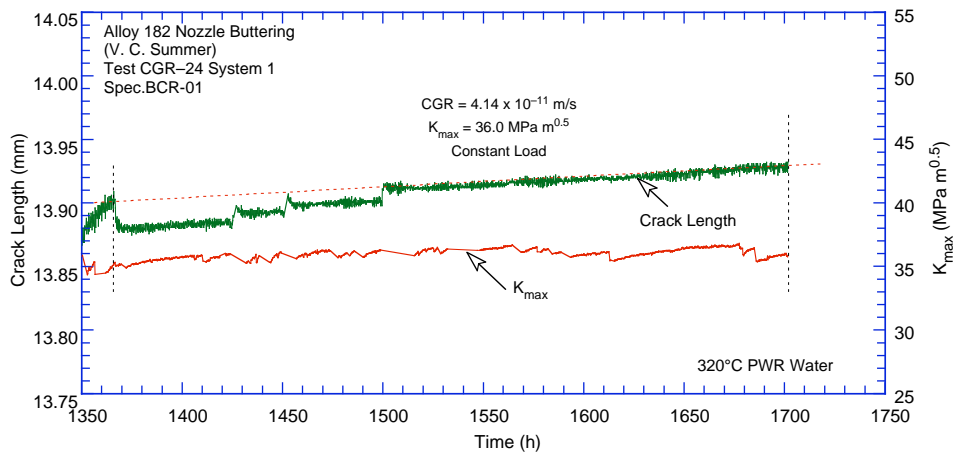
Figure 60. Crack length vs. time for Alloy 182 butter specimen in simulated PWR environment at 320°C during (a) precracking and test periods (b) 1, (c) 2–4, (d) 5–7, (e) 8–10, and (f) 11–12.



(d)



(e)



(f)

Figure 60. (Contd.)

At the conclusion of the test, the specimen was removed from the autoclave and prepared for fractographic examination. Figure 61 shows an image of the cross section of the BCR-01 specimen. The full extent of the crack was measured to be 1.848 mm (0.073 in.). The fracture surface was also examined by SEM to obtain an accurate measurement of the crack extent. Figure 62 shows the fracture surface of

Specimen BCR-01. Perhaps because of the different approach for the testing protocol with constant-load periods being separated by mechanical fatigue periods to physically mark the IG regions associated with each constant-load period, the difference between the measured crack length and that determined from the DC potential measurements was relatively small. The average crack extension was 1.980 mm (0.078 in.) compared with 1.472 mm (0.058 in.) determined from the DC potential drop method; i.e., a correction of 34%. The results shown in Table 16 and Fig. 60 have been corrected accordingly.

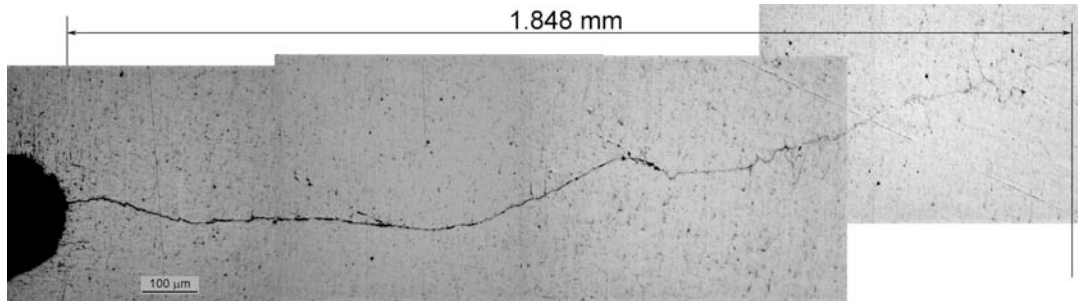


Figure 61. Cross section of the V.C. Summer Alloy 182 butter Specimen BCR-01.

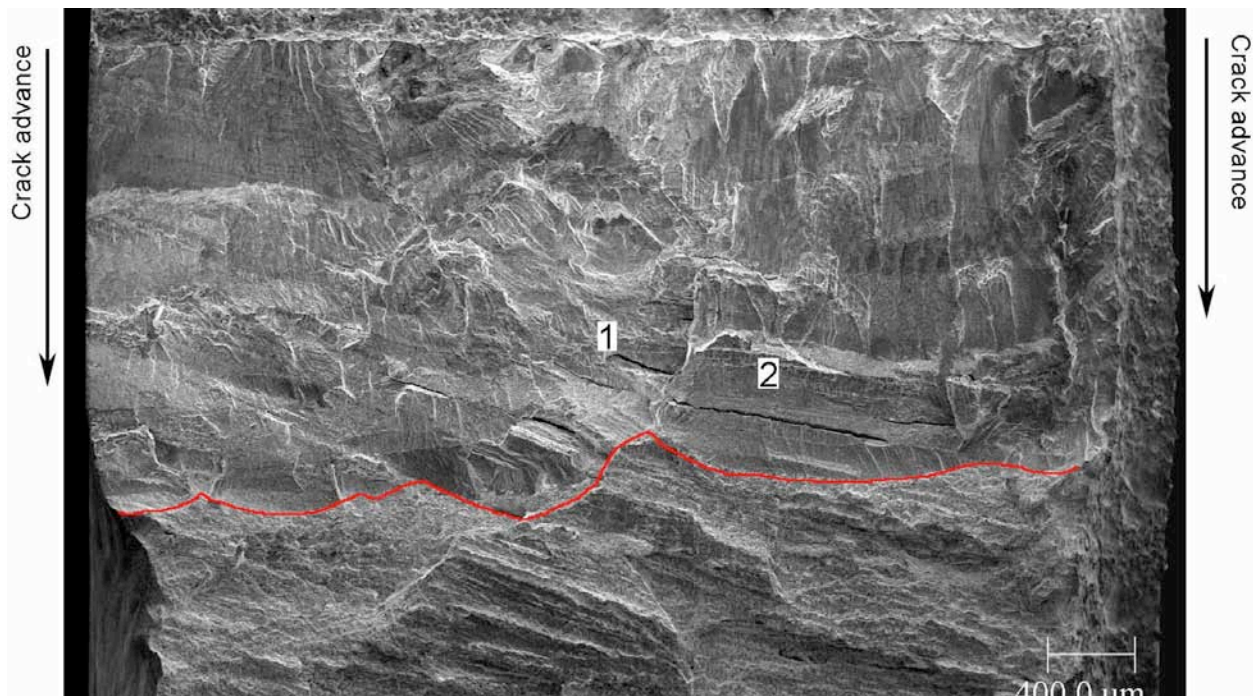


Figure 62. Micrograph of the fracture surface of Specimen BCR-01. Crack advance is from top to bottom.

As observed earlier for Specimen WCR-01, a fairly straight crack front was obtained for Specimen BCR-01 (red line in Fig. 62). Figure 63 presents two additional, high-magnification micrographs of the fracture surface taken at locations 1 (Fig. 63a) and 2 (Fig. 63b) in Fig. 62. In both micrographs, the IG fracture mode appears to be interrupted by crack branching, e.g., several secondary cracks, transverse to the crack plane, are observed along the crack front.

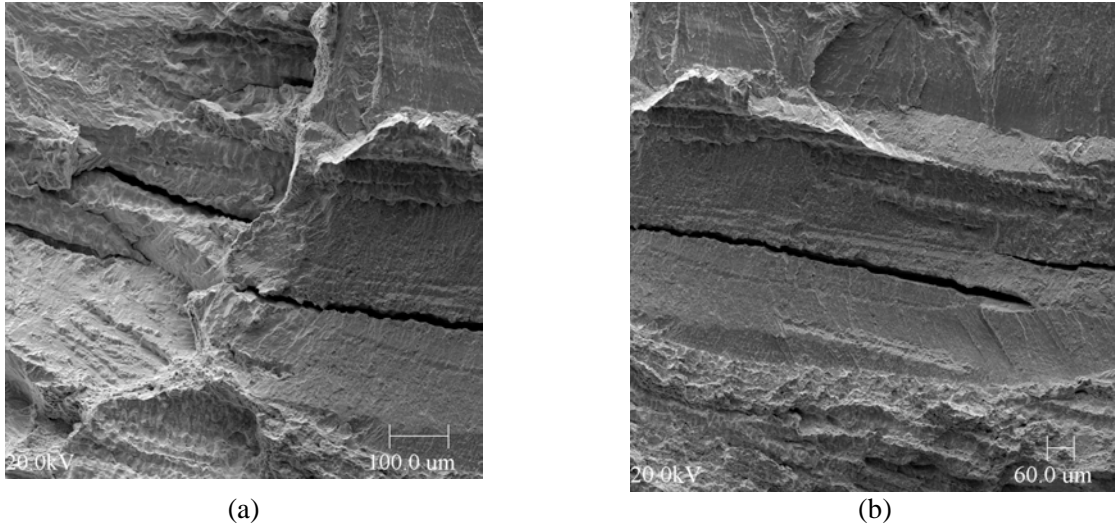


Figure 63. Micrographs of the fracture surface of Specimen BCR-01 at locations 1 (a) and 2 (b) in Fig. 62.

4.2.3.3 Specimen WLR-01

For this weld specimen, WLR-01, fatigue precracking was carried out at $R \approx 0.3$, $K_{\max} \approx 21.0 \text{ MPa}\cdot\text{m}^{1/2}$, and triangular waveform with 0.5–2 Hz frequency. R was then increased incrementally to 0.7, and the loading waveform changed to a slow/fast sawtooth with rise time of 50–1000 s. The crack growth data along with the test conditions, resulting stress intensity factors K_{\max} , and experimental and estimated CGRs for the two specimens are given in Table 17, and the changes in crack length and K_{\max} with time are plotted in Fig. 64.

Table 17. CGR data for Specimen WLR-01 of the Alloy 82 SMA weld in PWR water^a at 320°C.

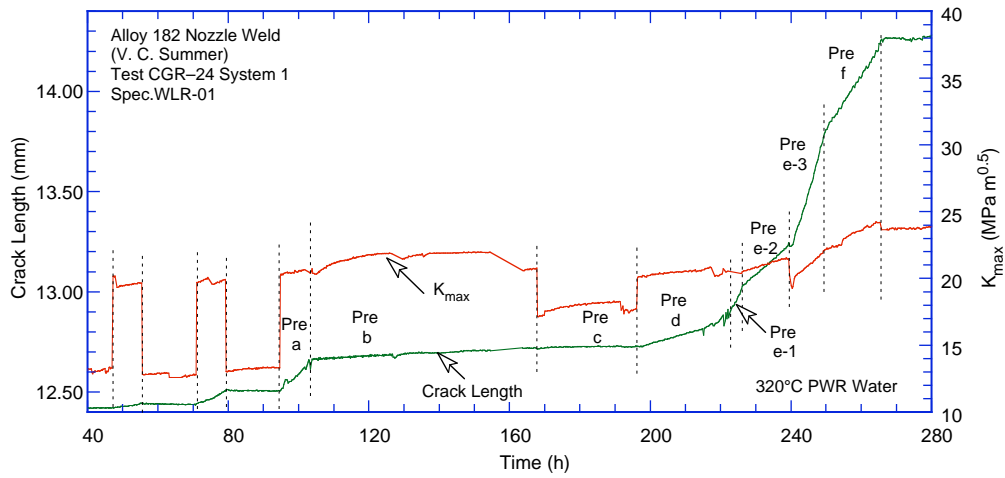
Test Period	Test Time, (h)	Cond, ^b (μS/cm)	O ₂ Conc., ^b (ppb)	Load Ratio R	Rise Time, (s)	Down Time, (s)	Hold Time, (s)	K_{\max} , ^c (MPa·m ^{1/2})	ΔK , (MPa·m ^{1/2})	CGR_{env} , ^d (m/s)	Estd. A182 CGR_{air} , ^d (m/s)	Crack Length, (mm)
Pre a	103	26	<10	0.30	0.5	0.5	0	20.92	14.64	8.22E-09	6.37E-08	12.640
Pre b	167	26	<10	0.30	50	2	0	20.77	10.38	2.61E-10	2.67E-10	12.719
Pre c	196	26	<10	0.30	1	1	0	17.72	8.86	1.35E-10	7.00E-09	12.729
Pre d	215	26	<10	0.30	0.5	0.5	0	20.84	10.42	2.82E-09	2.72E-08	12.837
Pre e	226	26	<10	0.30	0.25	0.25	0	20.43	14.30	1.20E-08	1.16E-07	13.017
Pre f	265	26	<10	0.50	1	1	0	24.44	12.22	1.52E-08	2.61E-08	14.251
1	315	26	<10	0.50	50	2	0	23.99	12.00	5.93E-10	4.78E-10	14.349
2	389	26	<10	0.69	1000	12	0	24.24	7.51	1.94E-10	6.86E-12	14.418
3	504	26	<10	0.67	1000	12	0	24.96	8.24	7.19E-11	8.92E-12	14.531
4	841	26	<10	1.00	–	–	–	24.67	–	2.07E-11	–	14.531
5	1082	26	<10	1.00	–	–	–	33.19	–	5.43E-12	–	14.590
6	1203	26	<10	0.70	1000	12	0	32.85	9.85	2.04E-11	2.20E-11	14.590
7	1392	26	<10	0.70	300	12	0	33.26	9.98	1.94E-11	7.71E-11	14.602
8	1398	26	<10	0.30	0.5	0.5	0	36.77	25.74	1.03E-07	6.40E-07	15.614
9	1417	26	<10	0.50	100	12	0	40.37	20.19	7.01E-09	2.05E-09	16.099
10	1439	26	<10	0.50	300	12	0	44.24	22.12	5.84E-09	1.00E-09	16.410
11	1466	26	<10	0.50	50	2	0	46.13	23.07	2.03E-09	6.95E-09	16.656
12	1531	26	<10	0.50	300	12	0	47.09	23.55	8.95E-10	1.25E-09	16.854
13	1634	26	<10	0.50	1000	12	0	49.15	24.57	4.12E-10	4.48E-10	16.964
14	2469	26	<10	1.00	–	–	–	52.50	–	7.71E-11	–	17.182

^aSimulated PWR water with 2 ppm Li, 1100 ppm B, and 2 ppm dissolved hydrogen ($\approx 23 \text{ cc/kg}$).

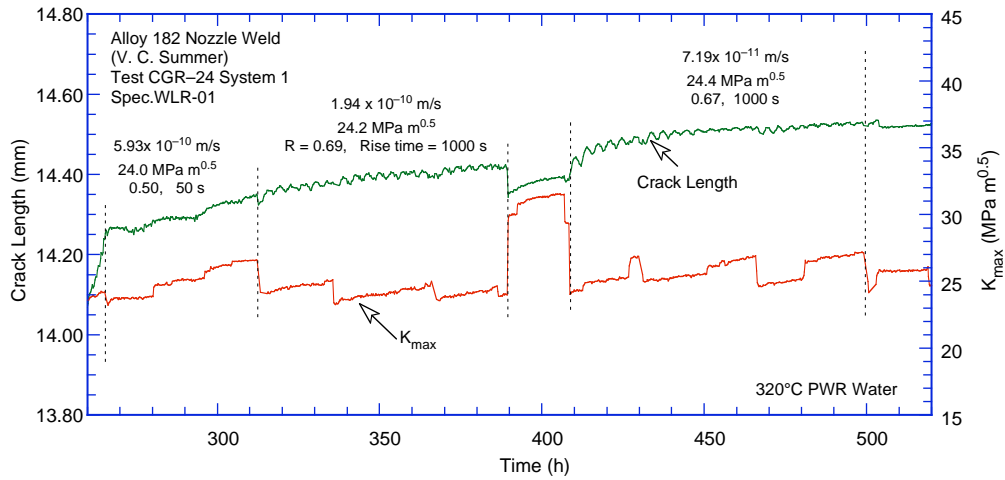
^bRepresents values in the effluent.

^cAt the end of the test, the maximum allowed K_{\max} was $22.6 \text{ MPa}\cdot\text{m}^{1/2}$.

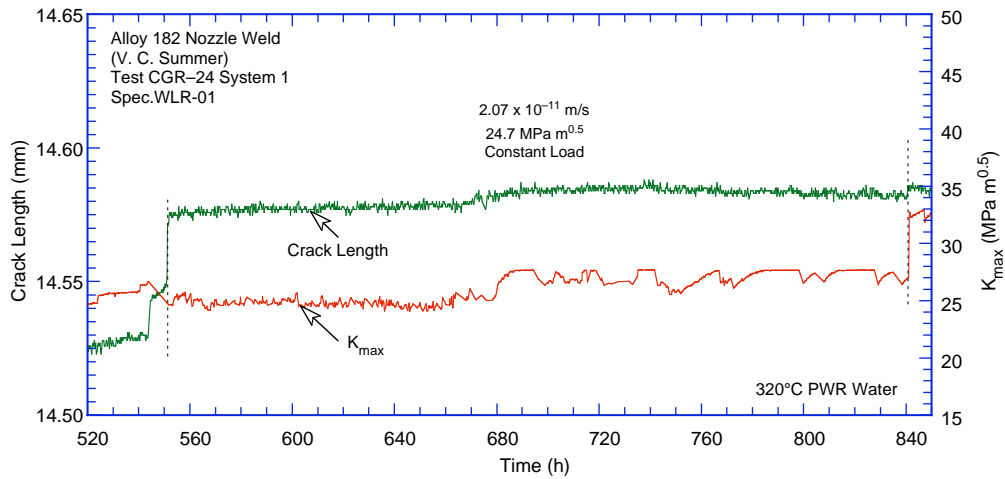
^dCrack growth rates for Alloy 182 weld metal in air determined by Eq. 14 in Section 5.1.



(a)

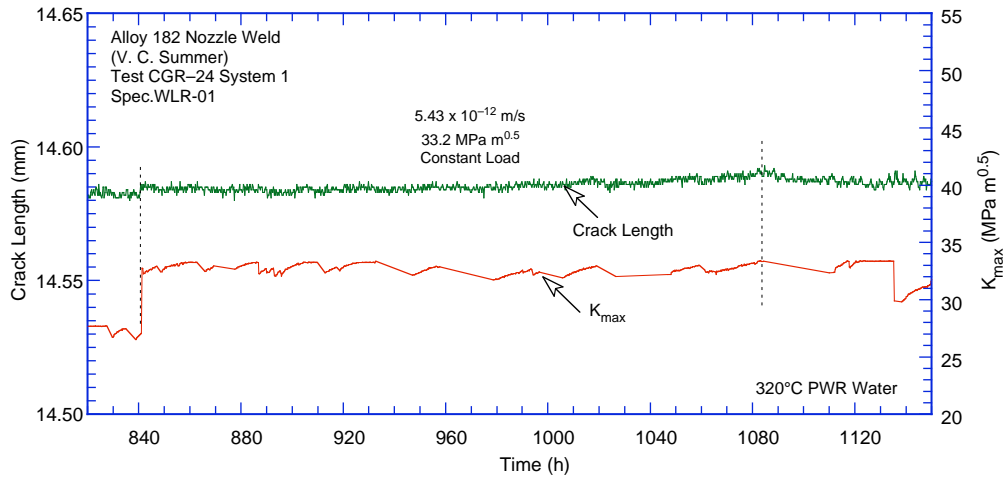


(b)

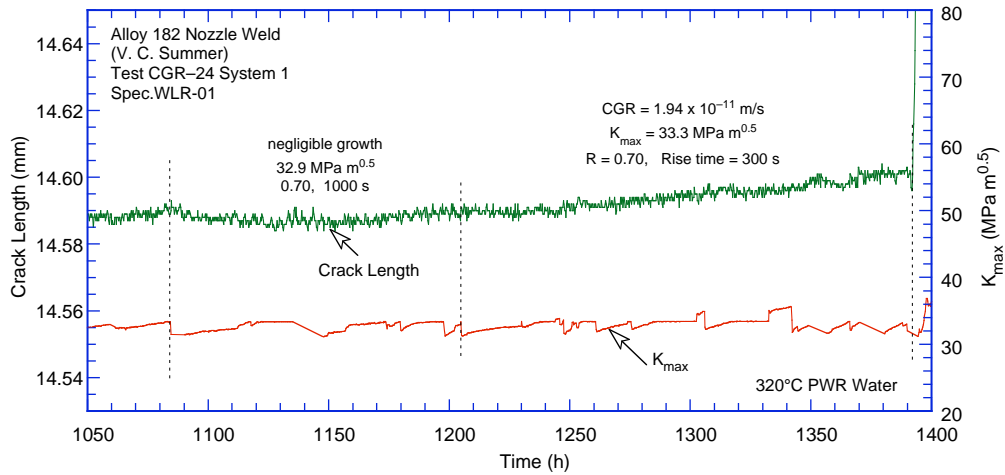


(c)

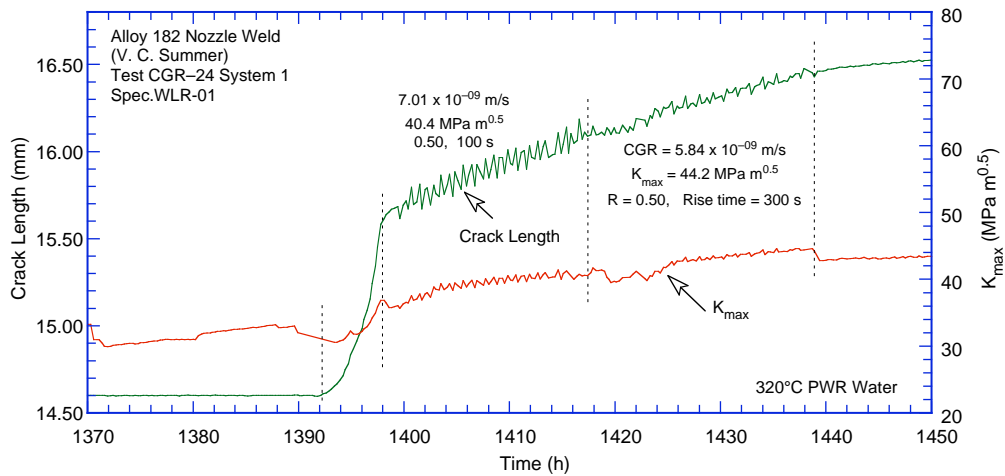
Figure 64. Crack length vs. time for Alloy 82 weld Specimen WLR-01 in simulated PWR environment at 320°C during (a) precracking, (b) precracking and 1–3, (c) 4, (d) 5, (e) 6–7, (f) 8–9, (g) 11–13, and (h) 14.



(d)

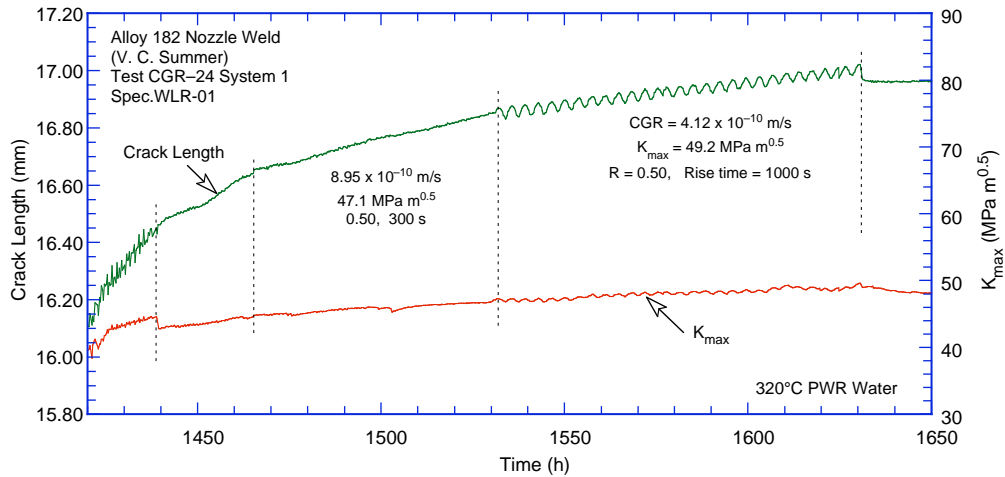


(e)

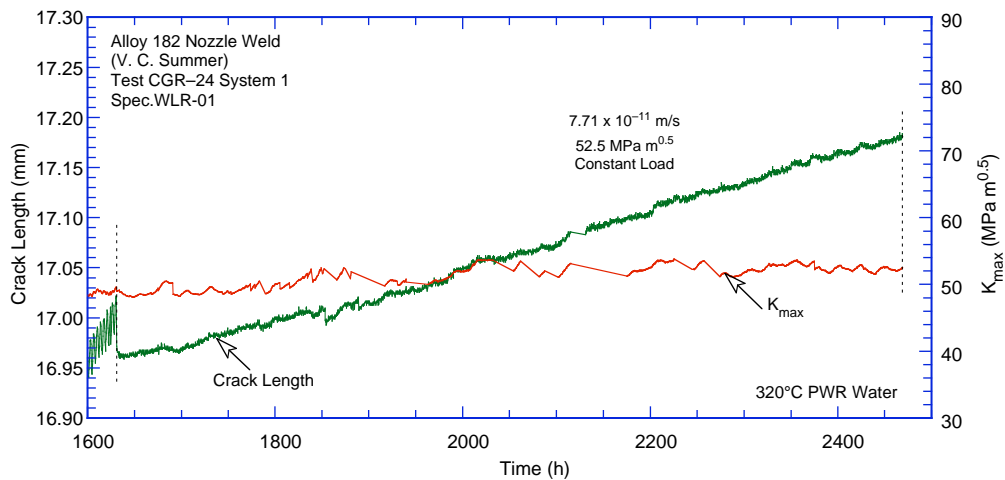


(f)

Figure 64. (Contd.)



(g)



(h)

Figure 64. (Contd.)

The fracture surface of WLR-01 is shown in Figs. 65 and 66. Cracking initiated in a TG mode under cyclic loading, changed to IG during the long rise-time periods of the test, and remained IG during the constant-load periods. Initiating the crack under cyclic loading and then transitioning to constant load with long rise-time cyclic loading seems to have resulted in a relatively straight crack front. The green and red lines mark the IG region. Secondary IG cracks were observed in the IG region, consistent with the previous observations on other V.C. Summer specimens. The IG region (green and red lines) was designated so as to encompass all these secondary cracks, based on the assumption that they initiated and grew during the constant-load period.

A comparison between DC potential data and measurements based on the SEM micrograph yielded correction factors of 1.69 for the TG region and 1.91 for the IG region. The relatively large correction factor for the TG region is consistent with the observation of some IG features within the TG region. The experimental conditions and corrected crack lengths are given in Table 17, and the changes in crack length and K_{max} with time based on the corrected results are shown in Fig. 64.